

Rapid compaction of granular material: characterizing two- and three-dimensional mesoscale simulations

J. P. Borg · T. J. Vogler

Received: 9 June 2012 / Revised: 3 October 2012 / Accepted: 8 November 2012 / Published online: 7 December 2012
© Springer-Verlag Berlin Heidelberg 2012

Abstract There have been a variety of numeric and experimental studies investigating the dynamic compaction behavior of heterogeneous materials, including loose dry granular materials. Mesoscale simulations have been used to determine averaged state variables such as particle velocity or stress, where multiple simulations are capable of mapping out a shock Hugoniot. Due to the computational expense of these simulations, most investigators have limited their approach to two-dimensional formulations. In this work we explore the differences between two- and three-dimensional simulations, as well as investigating the effect of stiction and sliding grain-on-grain contact laws on the dynamic compaction of loose dry granular materials. This work presents both averaged quantities as well as distributions of stress, velocity and temperature. The overarching results indicate that, with careful consideration, two- and three-dimensional simulations do result in similar averaged quantities, though differences in their distributions exist. These include differences in the extreme states achieved in the materials.

Keywords Shock compaction · Granular materials · Mesoscale simulations · Ceramics · Porosity

1 Introduction

The rapid compression of porous heterogeneous materials is of great interest when developing an understanding of a variety of processes including powder metallurgy, geophysical flows, ignition mechanisms in energetic materials, meteor impact and crater formation. Numeric simulations can provide information that cannot be obtained, or is not cost effective to obtain, from experimentation alone; this includes evaluating grain-on-grain interactions, hot-spot formation or large-scale parametric studies. It is common practice to model a heterogeneous material, such as a loose dry powder, as a continuum (i.e., the grains and porosity are treated as a new homogeneous single material) and assign average properties. In so doing the heterogeneous nature of the material and the grain interactions are lost. In continuum approaches of this type, additional constitutive relations such as the sphere collapse models [1], snowplow [2], P - α [3] and P - λ [4] are used to govern sub-grid behavior, namely, the removal of porosity.

With the continued development of massive computer architectures and parallel programming techniques, computational capabilities have improved such that sufficiently large domains and high-resolution simulations of these heterogeneous materials are feasible. The resulting simulations can utilize a large number of degrees of freedom in order to resolve each individual particle or grain during the compaction. Each grain within the powder is assigned the properties of the fully dense material. The simulation can then determine the macro-scale behavior, including the removal of porosity, without the use of additional constitutive laws. This approach is often referred to as a mesoscale (or middle scale) simulation because the intermediate micro- and macro-scales, those associated with the grain-level dynamics and the removal of porosity, are resolved.

Communicated by N. Thadhani.

J. P. Borg (✉)
Department of Mechanical Engineering, Marquette University,
1515 W. Wisconsin Ave., Milwaukee, WI 53233, USA
e-mail: john.borg@mu.edu

T. J. Vogler
Sandia National Laboratories, Livermore, CA 94551, USA
e-mail: tjvogle@sandia.gov

Several researchers have conducted numeric simulations utilizing a mesoscale approach. These studies ranged in complexity from resolving the shock and compaction interaction of tens to hundreds of grains in one and two-dimensional configurations to resolving thousands of grains in a three-dimensional configurations. Various computational techniques such as Eulerian hydrocodes, finite element or discrete element methods, have been used to resolve the dynamic evolution of a variety of heterogeneous and/or granular materials, including elemental metals and alloys [5–16], earth materials [17], energetic materials [18–32] and ceramic alloys [33–38]. These studies have demonstrated that mesoscale simulations can be used to successfully describe the compaction dynamics without the use of additional constitutive relations, while corroborating predictions from various analytic porous collapse models and experimental observations [8, 15, 39]. These mesoscale simulations, with idealized small-scale interactions, material constitutive laws and boundary conditions, have combined to resolve complicated features on the larger scales, such as the formation of dynamic force chains, void collapse and jetting, and hot spot formation. In most of these studies the focus was to numerically predict the averaged bulk material behavior, i.e., Hugoniot behavior or localized temperature.

Of considerable interest in the area of dynamic compaction is the formation and evolution of structured features such as force chains and hot-spots within heterogeneous energetic materials. To this end, several researchers have undertaken massively parallel three-dimensional simulations in order to understand this phenomenon [30, 40]. This work has demonstrated the importance of the three-dimensional nature of the heterogeneous flow and has identified that the thermal and mechanical states associated with the dynamic behavior of heterogeneous materials can be well described as a distribution of states or probability density function. This suggests a new approach to multiple-scale material modeling linking the mesoscale to continuum level descriptions via a statistical description. The associated effect of the role of force chains and the evolution of these distribution functions on the continuum behavior has yet to be fully understood.

The variation and complexity of the small-scale dynamics are vast, from non-linear constitutive behaviors and strength modeling, to chemical reaction and phase change, to complex morphologies and frictional interfaces. Several studies have incorporated inter-granular friction within the context of a mesoscale simulation in order to assess how grain level interactions affect the bulk response. For example, a discrete element method was used to investigate cylindrical wave propagation in discontinuous media with varying degrees of friction [41]. The results indicated that friction can have a pronounced effect on the velocity induced by the expanding wave. In an investigation of heterogeneous reactive materials, the importance of friction was characterized in the context

of hot spot formation [32]. This investigation concluded that hot spot formation was strongly enhanced by the presence of frictional heating. In the context of a projectile penetrating a granular material, mesoscale simulations were used to investigate the effect of frictional forces between the sand and the projectile [42]. The principal finding was that particulate heterogeneities results in an inhomogeneous loading of the projectile that causes projectile instability and trajectory change during penetration. In addition, this instability increases due to the presence of friction.

The work presented here seeks to further develop our understanding of the thermomechanical response of loose dry granular tungsten carbide (WC) when subjected to one-dimensional plane strain impact tests by utilizing two- and three-dimensional mesoscale simulations [35–37]. The aim is to assess differences between two- and three-dimensional simulations where porosity is explicitly incorporated. This will be accomplished by assessing differences in both averaged quantities such as the bulk longitudinal stress and temperature, as well as their distributions within the post compacted material. It is of interest to not only quantify the distribution of the thermomechanical state but to understand their evolution and underpinnings as related to the underlying material properties. In addition, of considerable interest in this work is to develop an understanding of the role of friction in the dynamic compaction of granular materials in a plane strain compaction experiment. Ultimately this work seeks to develop our understanding of dynamic processes associated with small-scale behavior and grain-on-grain interactions, and how these interactions effect the distribution of stress and temperature at a larger scale.

2 Computational setup

The dynamic compaction characteristics of porous granular single crystalline tungsten carbide (WC) powder (manufactured by Kennametal), with a characteristic grain length of 32 μm , have been experimentally investigated using one-dimensional flyer plate experiments [43]. Figure 1a presents an SEM image of the granular material of interest. The bulk material had an initial bulk density, ρ_{00} , of 8.56 g/cc with an initial volume fraction, ρ_{00}/ρ_0 , of approximately 55 %. Figure 1b presents a two-dimensional representation of the experimental test fixture utilized in the simulations investigated in this work, including the rigid driver plate, a granular collection of WC, a buffer plate and VISAR window. In order to simplify the computations, the impactor was not included in the simulations. Instead the cover plate was modeled as a rigid boundary with a specified velocity, similar to the boundary conditions utilized by others [5, 8].

In order to construct computational domains consisting of mono-dispersed randomly placed circles or spheres, a

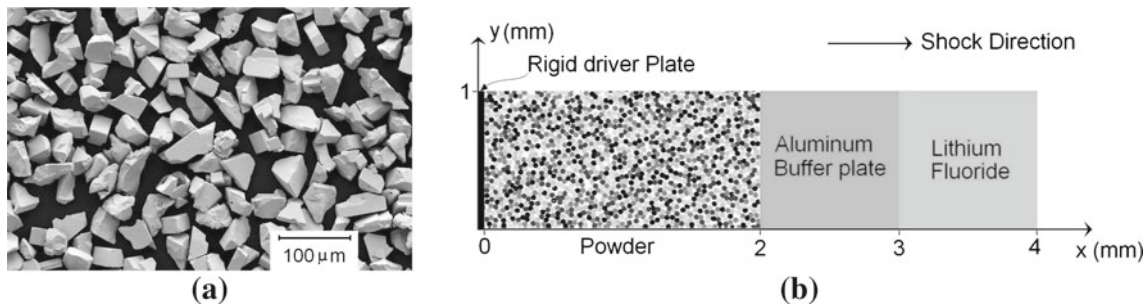


Fig. 1 **a** SEM image of tungsten carbide (WC) particles used in the experimental study and **b** two-dimensional computational geometry showing the computational domain utilized in this work

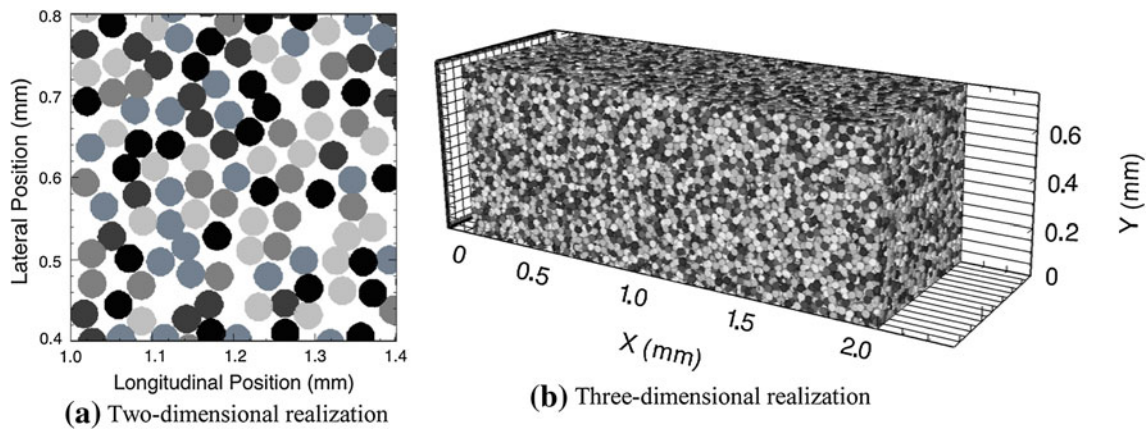


Fig. 2 Various initial material distribution of circular and spherical particles. Particles shading is for visualization purposes only

simple particle-packing algorithm was implemented. For a given computational domain, initial packing density and particle diameter (circle or sphere), including the number of grains required, is calculated. Grains, with zero initial radius, are placed at initial random seed locations throughout the domain. The grains are grown by incrementally increasing the diameter of each grain and allowing them to rearrange (pushing each other around as necessary with zero penetration) until the user specified diameter and packing density is obtained. For all of the simulations presented here the grains had a final uniform diameter of $32\ \mu\text{m}$. Figure 2a presents an enlarged view of grain realization presented in Fig. 1b illustrating the arrangement in two-dimensions; Fig. 2b presents the full domain in three-dimensions. Two-dimensional realizations were generated with mono-dispersed spheres as opposed to using slices of three-dimensional domains because previous work [36] in this area has indicated neglectable variation in the bulk response for a distribution of particles sizes.

Simulations were performed using two- and three-dimensional computational domains. The two-dimensional simulations were initially performed utilizing grain beds that were 1 mm tall (lateral direction) and 5 mm long in the shock direction (longitudinal direction). These match not only the

longitudinal length of the experiments but also domains utilized in previous simulations by the authors [35–37]. In that work it was reported that the average stress state achieved in the two-dimensional simulations was not affected by increasing the size of the domain in the lateral direction; the solution had converged in a bulk sense. However, in this work we have utilized two-dimensional domains that ranged from 1 mm tall to 18 mm. The three-dimensional simulations were performed utilizing domains that were 0.75 mm in both lateral directions and 2 mm in the longitudinal direction. The 3 mm tall two-dimensional simulations contained approximately 2,000 grains per mm along the longitudinal direction, whereas the three-dimensional simulations contained approximately 18,000 grains per longitudinal mm. The default two-dimensional simulations (5 mm longitudinal \times 3 mm lateral) contain just over 10,000 grains whereas the default three-dimensional simulations (2 mm longitudinal \times 0.075 mm \times 0.075 mm lateral) contain nearly 36,000 grains. The computational resolution was such that a minimum of 12 cells spanned each grain along a single coordinate axis. Periodic boundary conditions were utilized in the lateral directions.

Once the material distributions are generated, they are imported as initial conditions into CTH, a massively

parallel, Eulerian finite volume hydrocode developed by Sandia National Laboratories [44]. CTH was selected because of its long history in the shock community as well as its successful use in many applications including mesoscale simulations. Due to its numeric formulation however, realistic fracture, material interface tracking, and grain-on-grain contact dynamics are not treated realistically. The inability to model grain fracture might represent a significant deficiency since fracture may play an important role in the dynamic evolution of shocked ceramics [45]. Future studies will investigate the role of fracture by utilizing numeric schemes, such as peridynamic or finite elements, which incorporate fracture in a more direct and physical manner. In order to assess the deficiencies associated with unrealized intra-particle contact and friction laws we explored the effect of friction (stiction versus sliding rules) as outlined in the next section.

2.1 Sliding versus stiction

It was desired to explore the effect that grain-on-grain friction has on the overall dynamic bulk material response. Due to the Eulerian nature of these calculations, the grain interfaces are not resolved; thus friction is not a straightforward implementation of Coulomb friction at the particle interface. The effects of friction have not been implemented within CTH because techniques for its inclusion are currently not robust enough to handle strong shock loading [46]. Within a Eulerian formulation, grains that are touching, or very near to each other, will overlap within a single computational cell. If the two materials are different, the result is a so called mixed material cell. Within the CTH formulation, it is possible to specify the strength of mixed material cells. Thus when constructing the computational domain, care was taken to ensure adjacent grains were assigned different material numbers. In so doing, the interactions of mixed material cells at grain

interfaces and, therefore, grain-on-grain contact behavior can be controlled to a degree. The strength of a mixed cell can be either zero or a volume averaged fraction of the dynamic strength assigned to each material. Zero strength effectively enforces a non-penetrating, sliding interface between grains, i.e., no friction. However, this leads to grains surrounded by a thin layer of zero strength fluid which leads to large regions of material with zero strength, an unrealistic proposition. Alternatively, one can enforce a mixed material cell condition that sets shear gradients to zero within a single cell: *sliding*. This approximates the condition that the velocity is discontinuous across a sliding surface while retaining volumetric strength and a non-penetrating material boundary. This sliding condition is implemented in CTH via the SLIDE command. This condition effectively results in a granular material with no internal friction, an extreme condition to say the least.

The other extreme is to allow strength between neighboring particles by enforcing a volume averaged yield strength within mixed material cells, as was done in our previous two-dimensional studies [35–38]. This effectively weakly welds the initial grain realization. Using this approach we take advantage of the possibility that mixed material cells will not be completely filled and will thus contain voids. These partially filled mixed cells provide less strength than cells within the grains that are completely filled. As a result the interface between grains more readily yields. This in effect creates *stiction* between grains, i.e., intra-particle contact has strength until these cells exceed the local strength criteria at which point the cell yields according to the local flow rule or constant flow stress. The initial stiction strength is determined by the random grain realizations (due to the presents of voids), when inserting particles into a Cartesian mesh. Random grain realizations result in random distribution of stiction strength that varies along the contact surface between grains.

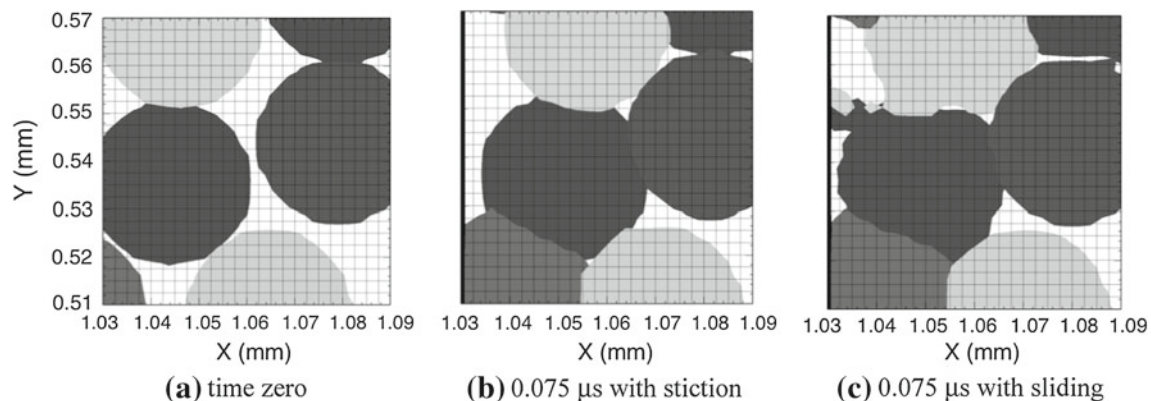


Fig. 3 Image of neighboring grains in a two-dimensional simulation at **a** time zero with the computational mesh superimposed. **b** and **c** illustrate post-shock grain deformation for stiction versus sliding, respectively

Table 1 Baseline material and constitutive constants

Parameter	WC [48,49]	Al ^a [50,53]	LiF [50,54]
Density, ρ (g/cm ³)	15.560	2.703	2.638
Zero stress shock speed, c_0 (km/s)	5.26	5.288	5.15
Hugoniot slope, s	1.15	1.3756	1.35
Grüneisen coefficient, $\Gamma = V(\partial P/\partial E)_V$	1.0	2.14	1.690
Specific heat, C_V (J/(g - K))	0.1723	0.8617	1.9217
Dynamic yield strength, Y (GPa)	5	n/a	0
Poisson's ratio, ν	0.20	0.28	0.50
Fracture strength, σ_s (GPa)	4.0	0.31	~ 0.01

^a Johnson–Cook visco-plastic model [51]

Figure 3 presents a view of several grains as they are compacted and the porosity is removed, for the stiction and sliding granular boundary conditions. Figure 3a presents the initial grain realization whereas Fig. 3b, c presents the post-compaction realization for stiction and sliding, respectively. The sliding results in more overall deformation and greater contact between grains.

2.2 Material constants

A Mie–Grüneisen equation of state was used for all materials included in these calculations [47]. The WC was modeled as linear elastic, perfectly-plastic with values for yield strength and Poisson's ratio obtained from Dandekar and Grady [48]. Experiments have indicated that the spall strength of hot-pressed WC declines rapidly with increased stress [48, 49]; spall strength decreases from a value of 2.06 to 1.38 GPa when shocked to 3.4 and 7.2 GPa, respectively. The range of shock stress of interest in this investigation varied from 1 to 4 GPa, thus considering the relatively modest shock stress levels of interest here, a constant value of fracture strength of 4 GPa was selected. The aluminum and lithium fluoride (LiF) equations of state parameters were obtained from the Steinberg compendium [50]. The aluminum (6061-T6) strength was modeled using a rate dependent Johnson–Cook visco-plastic model [51]. The fracture strength of the aluminum buffer plate was estimated from spall data presented in multiple sources [52, 53]. Given that the LiF is assumed to behave hydrodynamic, i.e., zero shear strength, the fracture strength was also assumed to be small. Material constants utilized for these calculations are listed in Table 1.

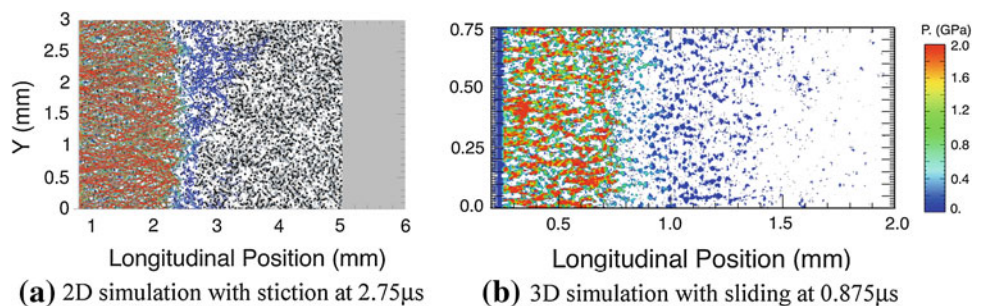
3 Results

The most pronounced feature associated with the dynamic compaction of heterogeneous granular materials is the variation in state generated within the material after the initial compaction wave passes. The compaction process does not result in a uniform state within the granular material; instead there are significant spatial variations behind the compaction wave.

Figure 4 illustrates the pressure as it propagates across the computational domain for two- and three-dimensional simulations. In both figures, the rigid driver plate has a specified constant particle velocity of 300 m/s traveling from left to right. Although the driver plate is planar, the compaction wave front within the granular material is not planar; instead the location of the compaction front varies as much as five particle diameters. This is similar to the several particle diameters fluctuations reported by Baer [21] for HMX and the stress distribution within the compaction wave fronts reported by Benson [7] for granular copper.

The characteristic feature of dynamically loaded heterogeneous materials is the existence of dynamically induced stress bridges, regions of high stress, aligned in the longitudinal direction. Stress bridges are evident in both two- and three-dimensional simulation, Fig. 4a, b. The formation, growth and development of these dynamic stress bridges (also known as force chains) are similar to those observed in quasi-static and weak shock simulations [54] as well as Hopkinson bar experiments on granular PMMA [55]. The formation of stress bridges observed here occurred over the entire range of driver plate velocities tested, 50 to 700 m/s. After compaction, the

Fig. 4 Two- and three-dimensional pressure plots for a driver plate velocity of 300 m/s. Plots illustrate the formation of stress bridges and wave front spatial variability



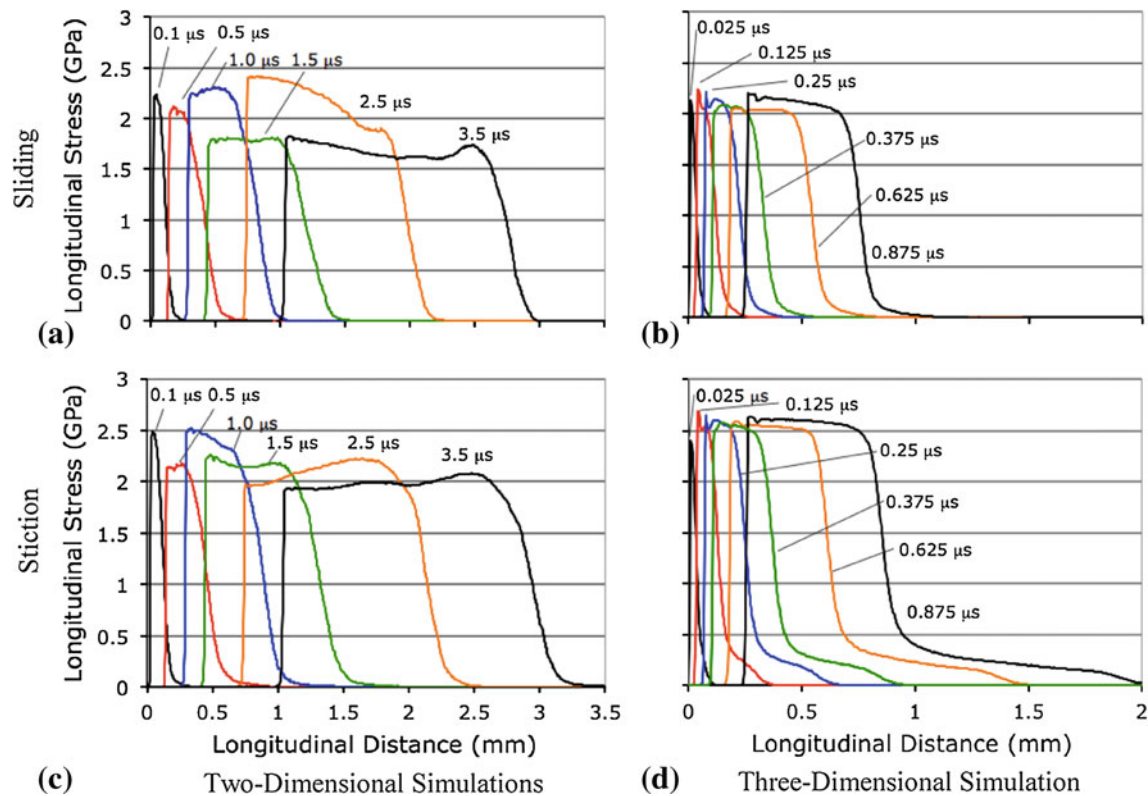


Fig. 5 Averaged longitudinal stress at various instances in time from two- and three-dimensional simulations illustrating the effect of grain stiction versus slide for a driver plate velocity of 300 m/s

stress bridges remain relatively stationary with respect to the distribution of material and advect with the flow, remaining relatively unchanged with respect to their magnitude. In the same way that a steady state of stress is achieved behind a planar shock, the dynamically induced stress bridges persist behind the compaction wave until they are perturbed by subsequent wave interactions. In these simulations the stress bridges persisted even after the re-shock from the back plate passes back over the granular material.

By comparing Fig. 4a, b, a distinguishing feature of two- and three-dimensional simulations can be observed. Namely, the three-dimensional simulations exhibit the transmission of more elastic behavior propagating ahead of the compaction front as compared to the two-dimensional simulations. This elastic behavior is supported by the three-dimensional nature of the grain realizations. In two-dimensional simulations there is no out of plane path for stress to be transmitted. Therefore an elastic wave cannot precede the compaction front to any significant degree; there is simply no connectivity to support such a breakaway effect and allow a two-wave structure. However, in a three-dimensional network of grains with 45 % porosity, nearly every grain is in initial contact with the grain network. The result is the possibility that an elastic wave can propagate through the network.

3.1 Averaged longitudinal stress time evolution

In order to quantitatively compare the simulation results, the longitudinal stress was averaged along the lateral direction(s) for the four different configurations of interest: two- and three-dimensions with either stiction or sliding. Figure 5 presents the results with a driver plate velocity of 300 m/s. With the inclusion of the times at which these averages were taken, it is interesting to compare these averaged profiles to the contour plots presented in Fig. 4.

A noticeable difference between the two- and three-dimensional simulations is the time (or distance) needed for the compaction wave to obtain a quasi-steady state stress. For the two-dimensional simulations with stiction, it is observed that the compaction wave required nearly 16 particle diameters before obtaining a quasi-steady compaction wave velocity, whereas two-dimensional simulations with sliding take considerably longer. Benson reported that two-dimensional simulations of Ni-alloy achieved steady behavior after a few particle diameters and that mono-size copper and alumina achieved steady behavior after 8 to 10 particle diameters [7,8]. It is worth noting that of these materials, alumina has the highest bulk sound speed, followed by tungsten carbide, nickel then copper. Thus the wave front thicknesses are somewhat correlated to the bulk sound speed.

Even after a quasi-steady wave velocity is achieved, significant fluctuations in localized stress can persist. In fact the overall spatial average at any given time can vary noticeably. As a result, it is difficult to discern when steady state is achieved by simply viewing the averaged stress profile. This is especially true at higher driver plate velocities (as will be shown in the next section), where stress localizations can cause the instantaneous average to deviate as much as 20 % from the overall averaged longitudinal stress associated with a given driver plate particle velocity. The three-dimensional simulations, however, achieve a steady stress state much more rapidly, on the order of 1.8 particle diameters and tend not to deviate from their average as much as the two-dimensional simulations. The quasi-steady state of stress behind the compaction wave for the three-dimensional simulations is much smoother compared to the two-dimensional simulations, although significant fluctuations still exist. In both the two- and three-dimensional simulations these fluctuations arise from the heterogeneous nature of the grain realizations, and specifically the formation and evolution of the stress bridges.

When comparing simulations, Fig. 5d, the average longitudinal stress for the two-dimensional stiction simulation is approximately 2 GPa, which is comparable to the average longitudinal stress achieved in the three-dimensional sliding simulation, Fig. 5a. The three-dimensional simulations with stiction results in higher average stress, near 2.5 GPa, and the two-dimensional simulations with sliding result in lower average stress, near 1.8 GPa. Thus the grain contact conditions (stiction versus sliding) can affect the average state of stress by as much as 20 %.

As discussed earlier, the three-dimensional simulations with stiction exhibit a precursor wave ahead of bulk compaction wave, Fig. 5d. This precursor wave is not present in either two-dimensional simulation or in the three-dimensional simulation with particle sliding. This implies that in order to sustain a precursor wave there must be a three-dimensional grain network and sufficient intra-granular friction to effectively transmit an elastic disturbance. This precursor wave, with an amplitude of approximately 0.4 GPa, travels at 2.3 km/s, which is nearly a third of the bulk wave speed, $\sqrt{K/\rho_{00}}$, of 5.1 km/s. With this said, it should be noted that experimental results obtained from VISAR signals did not indicate precursor wave behavior [43]. However, some minor precursors have been observed in sugar and soda-lime glass microspheres [31,57].

3.2 Average longitudinal, lateral and shear stress

In order to gain further insight into the complete state of stress within the grain network, the longitudinal, lateral and shear stress components were averaged in the lateral direction

over a range of driver plate velocities at a fixed longitudinal location and are presented in Figs. 6 and 7 below.

3.2.1 Two-dimensional simulations

Figure 6a, b presents the averaged longitudinal stress from the two-dimensional simulations with the driver plate velocity varying from 100 to 600 m/s. The profiles have been selected such that the leading edge of the compaction wave has reached the same longitudinal position. As the driver plate velocity is increased, so too is the averaged longitudinal stress. An obvious feature of these profiles is the presence of oscillations in the post compaction state with wave length, λ . The frequency of these oscillations increases as the driver plate velocity is increased. This is especially true once the average stress in the grain network exceeds the dynamic yield strength of the material, 5 GPa.

The averaged lateral stress is presented in Fig. 6c, d. For a given drive plate velocity, the average lateral stress is lower than the average longitudinal stress until the averaged longitudinal stress exceeds the dynamic yield strength, after which the two are nearly identical. The average lateral stress exhibits much shorter wavelength oscillations, λ_T , in the post-compaction state as compared to those observed in the longitudinal stress profile. The relationship between the longitudinally aligned stress bridges and the behavior of the longitudinal and lateral stress is not well understood. In order to gain a better understanding of this and the role of stress bridging, the stress distributions will be explored in greater detail in Sect. 3.6.

The deviatoric shear stress components fluctuate about zero for all simulations performed in this work, therefore the averaged shear stress is zero. Thus Fig. 6e, f presents the average of the absolute value of the xy deviatoric shear stress component for each cell. The characteristic shape of the average deviatoric shear stress profile is similar for all the driver plate velocities: a large increase as the compaction wave passes, followed by a decrease and leveling off to a constant value near 0.5 GPa. The longitudinal thickness of the large shear stress peak is approximately 0.5 mm which roughly corresponds to the distance the compaction wave requires to achieve a steady wave profile. Thus the peak in the average absolute value of shear stress is associated with the compaction wave thickness, grain re-arrangement, local yield and slip as the compaction wave achieves a steady profile. In addition the amplitude of the shear stress peak for stiction grains is larger than the sliding grains. This is to be expected for a welded grain network where shear stress can be more readily transferred from grain to grain.

One final observation from Fig. 6a, b is the structure of the post-compaction stress state for the stiction as compared to the sliding. For example, compare the locations of the peaks and valleys with respect to the longitudinal position

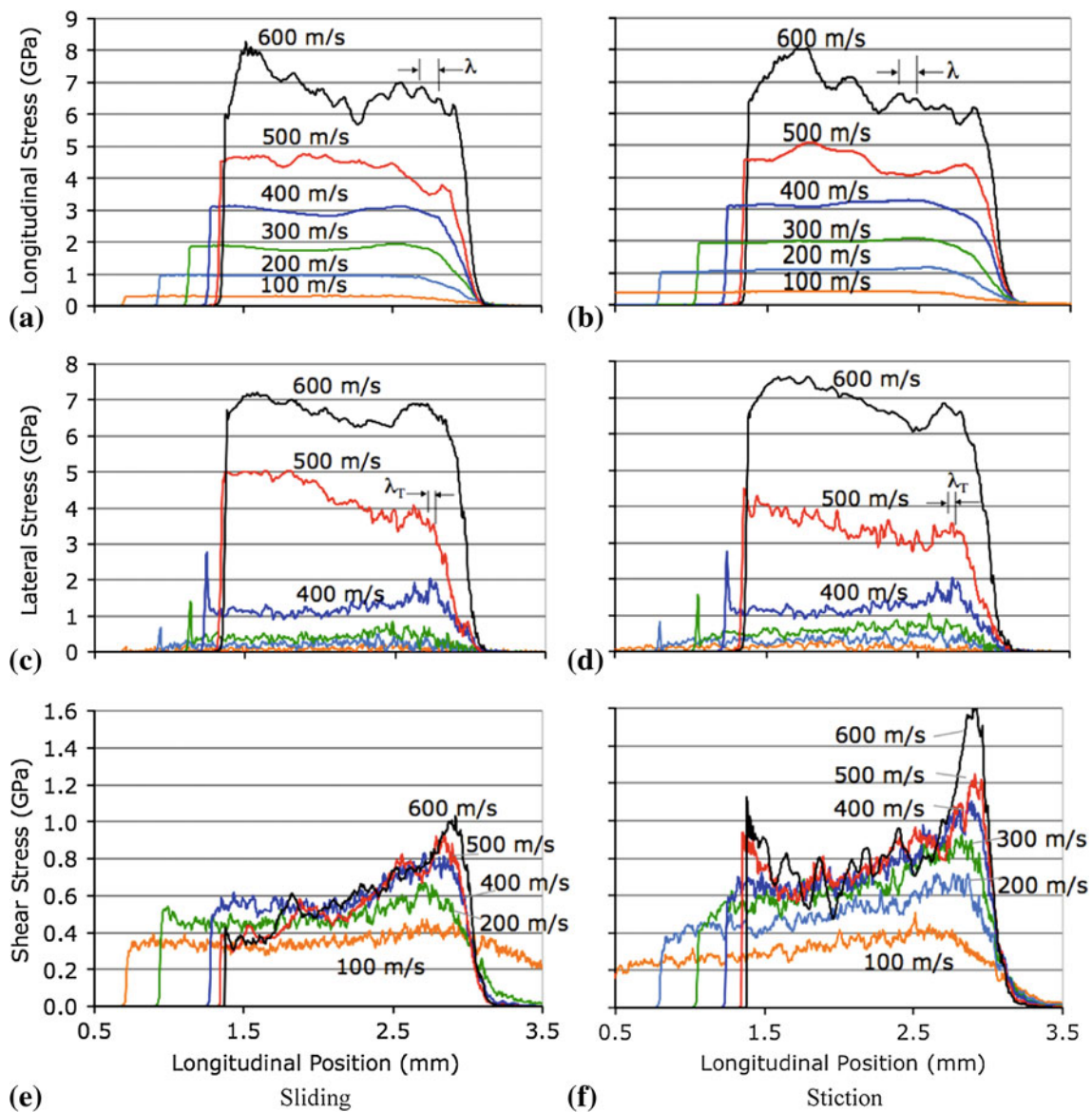


Fig. 6 Averaged components of stress tensor from two-dimensional simulations for both particle stiction and sliding for various driver plate velocities. Oscillations within post-compaction state of the material dif-

fers in the longitudinal direction, λ , as compared to the longitudinal direction, λ_T

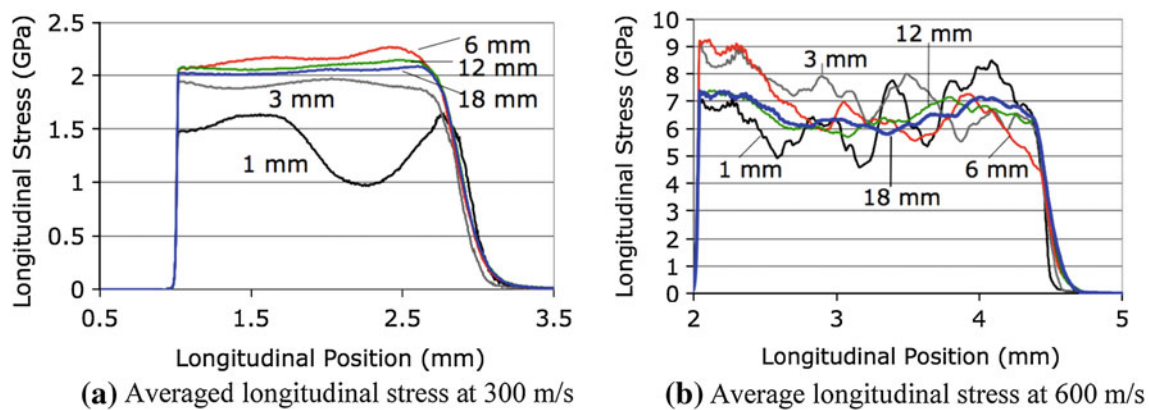


Fig. 7 Averaged longitudinal stress profiles for two-dimensional simulation with sliding as a function of domain height for two different driver plate velocities

for stiction and sliding simulations for a driver plate velocity of 600 m/s. The peaks and valleys in stress appear at the same longitudinal position for simulations with either stiction or sliding particle contact conditions. This implies that the variation in stress behind the compaction front is dependent upon the particle realization and specifically to the local heterogeneity of the realization. This correlation persists, to a lesser degree, as the driver plate velocity is reduced. Thus we conclude that post compaction fluctuations (λ and λ_T) observed in these simulations are, in large part, due to local heterogeneity.

In order to explore the variation in the post-compaction stress, the lateral size of the domain of the two-dimensional simulations was increased from 1 to 18 mm while keeping the grid resolution constant; the results for one instant in time are presented in Fig. 7. At 18 mm there are as many grains (and computational cells) in the two-dimensional simulation as there are in the three-dimensional simulation. The results indicate that as the lateral domain size is increased the post compaction stress becomes smoother. However, even with an increase in longitudinal height of the domain, the post shock oscillations have not been completely eliminated.

Although the average longitudinal stress appears to vary as the domain size is increased, one should keep in mind that these profiles represent one instant in time. In fact, the average longitudinal stress can vary from instant to instant; this is especially true of the smaller domains. As it happens the snap shot presented in Fig. 7a indicates the average is low compared to the other domains. However, if the longitudinal stress is averaged behind the compaction wave, over a series of snap shots in time, the average stress for simulations with longitudinal heights from 1 to 18 mm is approximately 2 GPa.

3.2.2 Three-dimensional simulations

Figure 8 presents the longitudinally averaged stress profiles from the three-dimensional simulations. When comparing the two- and three-dimensional wave profiles the most obvious feature is the overall smoothness of the averaged three-dimensional simulations as compared to the two-dimensional simulations. The two-dimensional simulations result in post compaction longitudinal stress characterized by low frequency undulations. By contrast, the three-dimensional simulations result in much smoother averaged stress across the entire range of driver plate velocities investigated. This is especially true of the lateral and shear stress profiles.

As previously noted, the three-dimensional simulations with stiction support an elastic precursor wave, whereas the other simulations do not. When these three-dimensional simulations were initially performed the longitudinal grain bed thickness was 1 mm long. This shorter distance allowed the precursor wave to quickly interact with the back plate, effectively re-shocking the compaction wave before it had propa-

gated sufficiently into the grain bed. This re-shock behavior made the results difficult to interpret. Once the particle bed thickness was increased the two-wave behavior was obvious. Thus care must be taken to insure simulations are sufficiently long to distinguish the compaction and precursor wave behavior.

Although three-dimensional simulations with grain stiction exhibit precursor behavior in the longitudinal stress, the corresponding averaged lateral stress profiles do not. The position of the average lateral stress wave corresponds to the position of the average longitudinal stress wave. Given the relatively low Poisson's ratio of WC, this result is not surprising.

The averaged lateral stress for the three-dimensional simulations with sliding exhibits some distinguishing features from its stiction counter-part. Most notably, at low driver plate velocities the averaged lateral stress is negative, i.e., the average particle is in tension with respect to the lateral direction. As the driver plate velocity is increased the average lateral stress is increased.

Like the two-dimensional simulations the averaged deviatoric shear stress is zero, thus the average absolute value of the deviatoric shear stress was calculated and presented in Fig. 8e, f. The presence of the precursor wave is apparent for the simulations with stiction. At high driver plate velocities, near 400 m/s, the averaged shear stress from the three-dimensional simulations exhibits the same waveform as seen in the two-dimensional simulations: namely, an initial peak in shear stress followed by a decay to a near constant value behind the compaction front. As was observed in the two-dimensional simulations, the peak amplitude of the deviatoric stress is higher for the stiction simulations as compared to the sliding simulations. This is to be expected for a welded grain network where shear is more readily transferred.

3.3 Bulk response

In order to compare the averaged bulk behavior to experimental data, the post compaction longitudinal, lateral and shear stress values from the simulations are plotted versus density in Figs. 9 and 10. The data was obtained by averaging the data presented in Figs. 6 and 8. Experimental data, as well as the full dense WC Hugoniot, have also been presented for comparison [43].

For the two-dimensional simulations, both the stiction and sliding grain boundary conditions under predict the experimental response; the sliding grains under predicts more so than the stiction grains. In previous work it was demonstrated that the bulk response utilizing a two-dimensional stiction configuration can be increased to that of the experimentally measured response by increasing the dynamic yield strength of the solid WC from 5 to 8 GPa [36]. The two-dimensional

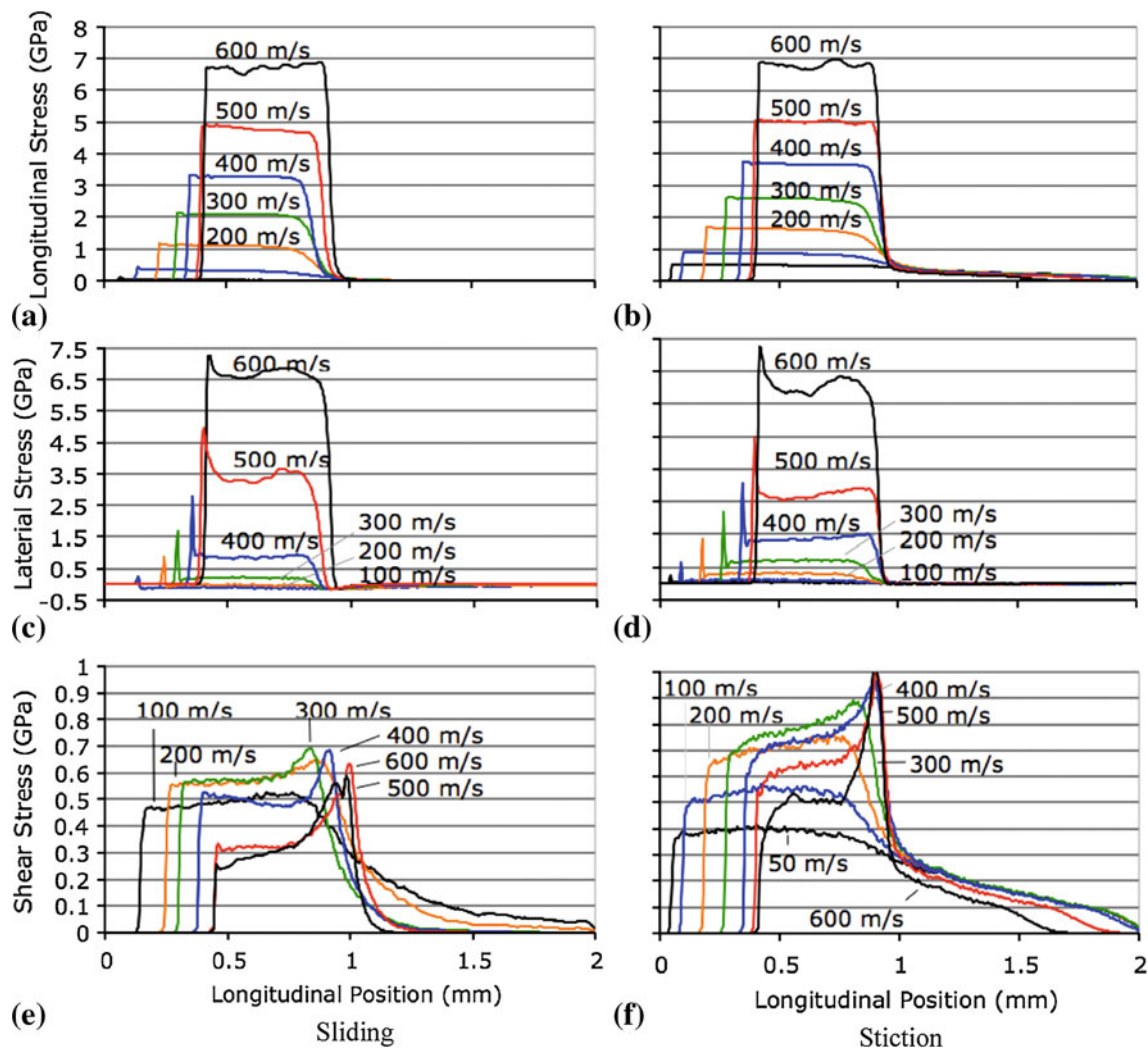


Fig. 8 Averaged components of stress tensor from 3D simulations illustrating the effect of particle stiction versus particle slide for various driver plate velocities

simulations, as well as the sliding three-dimensional simulation, intersect the bulk Hugoniot at approximately 5 GPa, which corresponds to the dynamic yield strength of the solid WC, see Table 1. Where the bulk response of the granular material intersects the solid Hugoniot indicates the state at which all of the porosity is removed. Thus these simulations predict that the porosity is completely removed when subjected to a compressive stress equal to the dynamic yield strength of the solid constituent material. Interestingly, the three-dimensional simulation with stiction requires significant higher stress to completely remove the porosity. This is due to localization of stress facilitated by grain stiction.

As a result, the three-dimensional baseline simulations with stiction over predict the bulk response, whereas the sliding grain condition under predicts the bulk response. The experimentally bulk response lies between the three-dimensional sliding and stiction grain conditions. Thus it

appears that some degree of grain stiction and sliding is necessary in order to reproduce the experimentally determined bulk response.

It is interesting to note that the bulk response from the two-dimensional stiction simulations results in nearly the identical response as the three-dimensional sliding simulations. Thus the out-of-plane rigidity provided by the three-dimensional interlocking grain network can be simulated by initially welding the particles network in a two-dimensional simulation. That said however, both slightly under predict the bulk response.

The plots presented in Fig. 9 indicate that the averaged lateral stress is fairly constant over a wide range of compaction states but sharply rises near full compaction. In addition the absolute value of the average shear stress initially increases with increasing driver plate velocity but decreases as the lateral stress rises sharply. Thus at high driver plate velocities

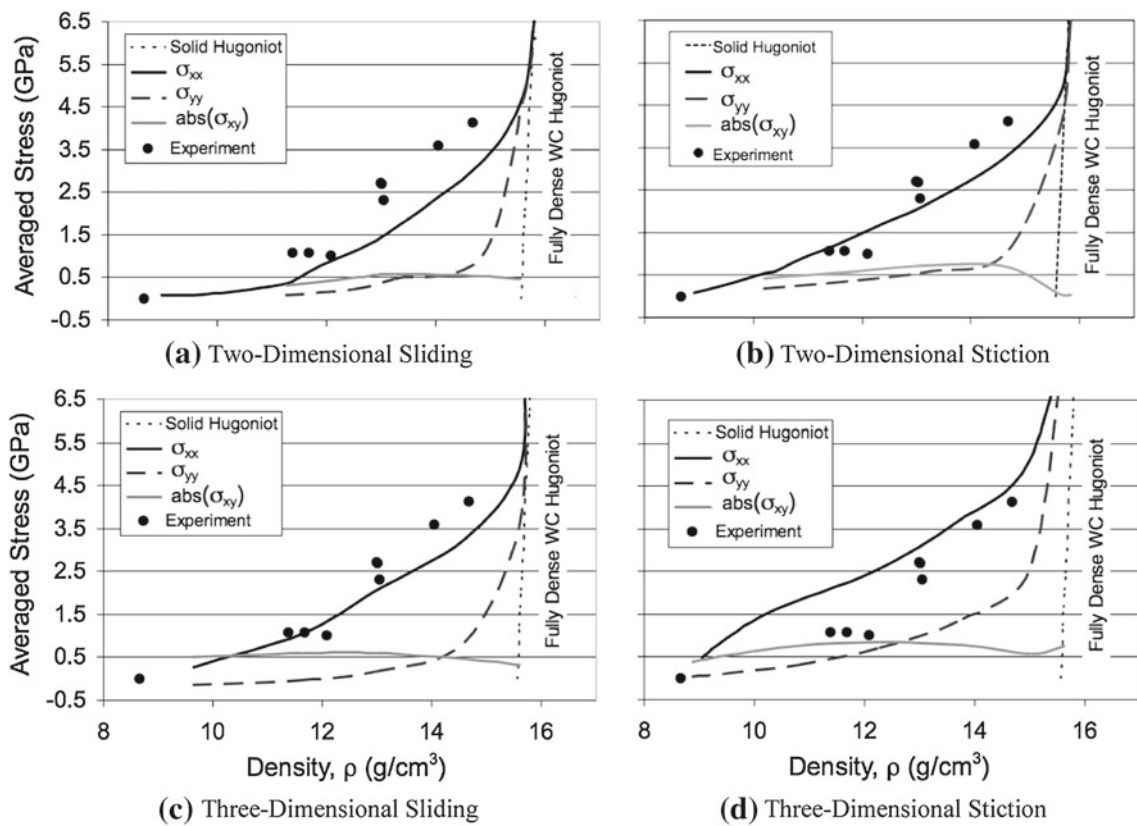


Fig. 9 Bulk dynamic response of two- and three-dimensional simulations with stiction or sliding

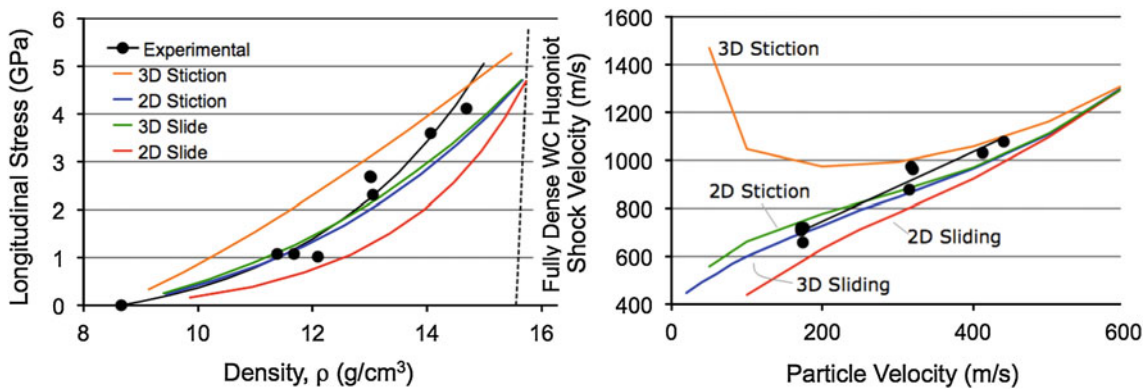


Fig. 10 Average longitudinal stress compared to experimental data

the state of stress within the grain network moves towards a hydrodynamic state of stress.

In order to compare the differences in the two- and three-dimensional simulations, the Hugoniot states in stress-density and shock velocity-particle velocity space are presented in Fig. 10. As was done in previous work, this data was obtained by averaging the compaction wave speed (shock speed) through the granular material; the stress-density states were obtained via the jump conditions [35,36].

The presence of the elastic wave in the three-dimensional stiction wave profiles presented in Fig. 8b results in rela-

tively high shock speeds at low particle velocities. At the lowest particle velocities it is difficult to distinguish the elastic precursor wave from the compaction wave. The result is an apparent increase in the shock velocity as particle velocity is decreased. As the particle velocity goes to zero the shock velocity would appear to approach 2.3 km/s, the elastic precursor wave speed.

As stated above the three-dimensional stiction results are stiffer than the experimental data, whereas the two-dimensional sliding results are softer than the experimental data. The two-dimensional stiction and three-dimensional

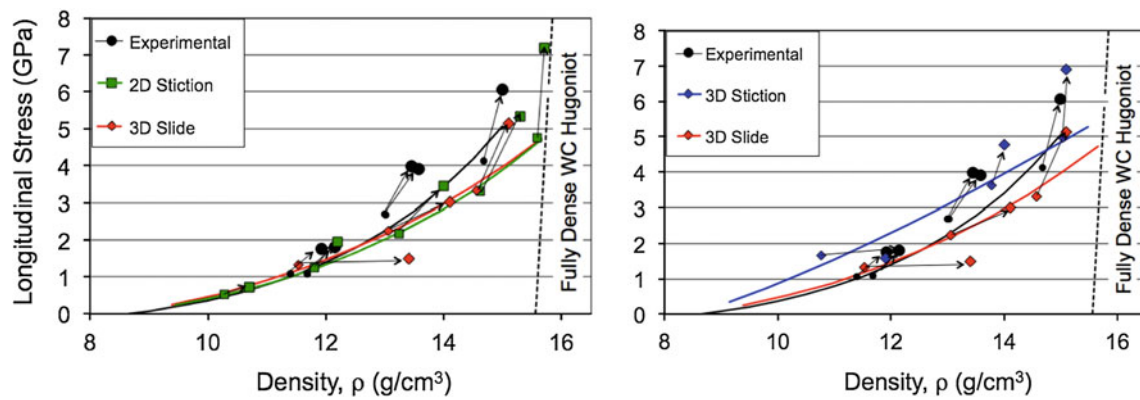


Fig. 11 Simulated shock and reshock response compared to experimental data. The *arrows* indicate the transition from initial shock Hugoniot state to reshock state

sliding results better fit the experimental data at lower stress, whereas the three-dimensional results better fit the experiments at high stress. The two-dimensional stiction and the three-dimensional sliding Hugoniot are nearly identical to each other across the entire range of compaction. These results would indicate that two-dimensional models, with the correct mesoscale behavior, can be used to simulate the bulk compaction behavior as accurately as three-dimensional simulations.

3.4 Reshock

When the compaction wave reaches the higher impedance aluminum buffer plate, a reshock wave is reflected back into the WC. This reshock, which can be resolved experimentally, gives another opportunity to compare experimental and simulated data. The density and stress of the reshock grain system is presented in Fig. 11 along with data from the experiments; the respective Hugoniot are drawn as solid lines. Each shock and reshock is indicated as a pair of points connected by an arrow illustrating the transition from shock to reshocked, respectively. The experimental data indicates that the reshocked states rise above the initial shock Hugoniot.

Figure 11a presents the simulated results that best matched the experimental Hugoniot data: two-dimensional stiction and three-dimensional slide results. The reshock states rise above the shock Hugoniot at high stress levels but not at low stress levels. The stiction versus sliding conditions do not appear to have much of an effect on the reshock behavior. Figure 11b presents the three-dimensional sliding and stiction results. The reshock behavior of the three-dimensional stiction simulations is steeper compared to the sliding simulations; the experimental response appears to be between the two. Both of the three-dimensional simulations tend to re-compact easily at low stress levels; the reshock stress only slightly increases for large increases in density.

3.5 Rise times

In order to further explore the differences between two- and three-dimensional simulations the relationship between longitudinal stress and strain rate was explored. Swegle and Grady observed that the shock profile can be described by a power law relationship, $\dot{\epsilon} = \sigma^n$, where σ is the applied longitudinal stress (Hugoniot stress) and $\dot{\epsilon}$ is the strain rate associated with the shock front [58]. For a broad range of fully consolidated brittle and ductile materials, this relationship is fourth order, i.e., the exponent n is 4. Zhuang et al. [59] studied samples of polycarbonate layered with aluminum, stainless steel, and glass, finding a relationship of strain rate scaling with stress to the second power. However, studies of dynamic compaction of granular materials such as tungsten carbide, sand, titanium dioxide, and sugar have found strain rate to scale with stress to the first power [38, 43, 60, 61].

The simulations described here were used to fit the stress–strain rate power relations in two longitudinal locations. The first fit was obtained from averaged longitudinal stress profiles taken within the powder, Fig. 12a. This was done in order to characterize the variation within powder during compaction. Figure 12b presents the averaged results in which the trend are more easily discerned. A second fit was obtained from data taken within the aluminum buffer. This was done in order to follow the experimental methodology and to assess the effect the aluminum buffer plate has on the results.

In order to fit the power law relationship, the average longitudinal stress (Hugoniot stress) was obtained from Fig. 10. The strain rate was obtained by dividing the volumetric strain by the rise time: $\dot{\epsilon} = \epsilon / \Delta t = u_p / U_s / \Delta t$. The rise time was obtained from each averaged stress profile at an instant in time either within the powder (Figs. 6 or 8) or the aluminum buffer. The rise time was calculated by first finding the slope of a straight-line fit through the stress profile at 20 and 80 % of the Hugoniot stress. The associated characteristic rise time, Δt , was calculated by extrapolating the time required for

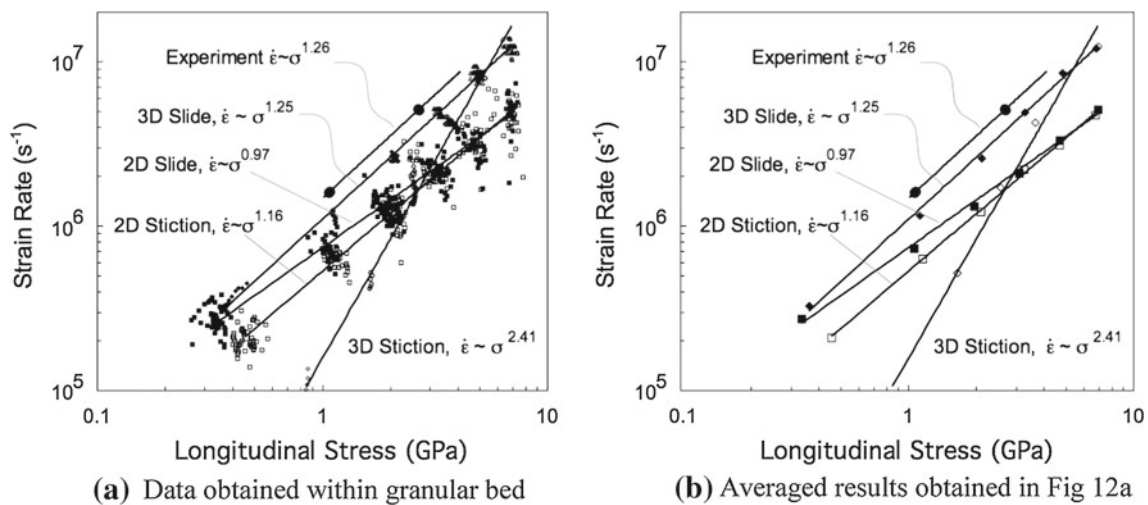


Fig. 12 Stress–strain rate relationship for two- and three-dimensional simulations with either stiction or sliding

this straight-line fit to go from zero to the Hugoniot stress. The results are presented in Fig. 12 along with experimental data [43].

Since the compaction wave speed and amplitude vary as the compaction wave propagates through the granular material, there exists a significant degree of scatter in the stress–strain rate data presented in Fig. 12a. This is especially true of the two-dimensional simulations as compared to the two-dimensional simulations.

The results presented in Fig. 12b indicate that the three-dimensional sliding simulations replicate the experimentally determined stress strain-rate exponent whereas the stiction results over predict the exponent. The two-dimensional simulations both slightly under predict the exponent, however the two-dimensional stiction results come close to the experimental result. As observed in the three-dimensional simulations, the profiles with stiction are stiffer than the profiles with sliding.

Finally, the wave front profiles were reanalyzed after they passed into the aluminum buffer plate. It was found that the wave steepened as it propagates through the aluminum buffer. The simulations indicate that the stress–strain rate exponent increases by 0.4 after traversing 0.5 mm within the aluminum buffer. With the knowledge of this behavior of the buffer material, one can correct for this steepening as has been done previously [43].

3.6 Distributions in stress profiles

Based on better agreement of the two-dimensional stiction and the three-dimensional slide we will focus on those two cases going forward. In addition to the average stress states (i.e., the Hugoniot state) distributions of states can also be important. A good example is energetic materials and their sensitivity to hot spot formations. Although ignition obvi-

ously cannot occur in WC, energetic materials have frequently been the subject of both two- and three-dimensional simulations. Figures 13 and 14 present distributions of the wave stress profile as a function of longitudinal position at various driver plate velocities for the two- and three-dimensional simulations. These figures, the averages of which were presented in Figs. 6 and 8, present what are essentially distributions of stress, or contours, as a function of longitudinal position for one instant in time; the higher the occurrence the darker the shaded area. These plots visualize the compaction process in two novel ways. First, they demonstrate the relationship between the most likely occurrences of stress (the darkest shading) relative to the average stress (the solid red lines). It is clear that the average stress does not necessarily lie on the most likely occurrence of stress. In nearly all cases the average longitudinal stress lies between the most likely occurrence and zero stress. This indicates the emergence of a bi-modal distribution that is associated with the formation of stress bridges. The grains involved in the stress bridge experience greater stress while those outside the stress bridge network experience little to no load. The differences between most likely occurrence and average are more pronounced at low to intermediate driver plate velocities between 200 and 500 m/s, where a significant number of cells experience stress in excess of twice that of the average stress. As the driver plate velocity is increased and porosity is completely removed, there are fewer occurrences of zero stress behind the compaction front. The behavior of the bi-modal stress distributions will be explored in greater detail in the next subsection.

The second interesting feature of these plots is that they demonstrate the spatially varying nature of the compaction wave and the formation of a compaction rearrangement region. There are significant deviations in the most likely occurrence of stress near the leading edge of the compaction

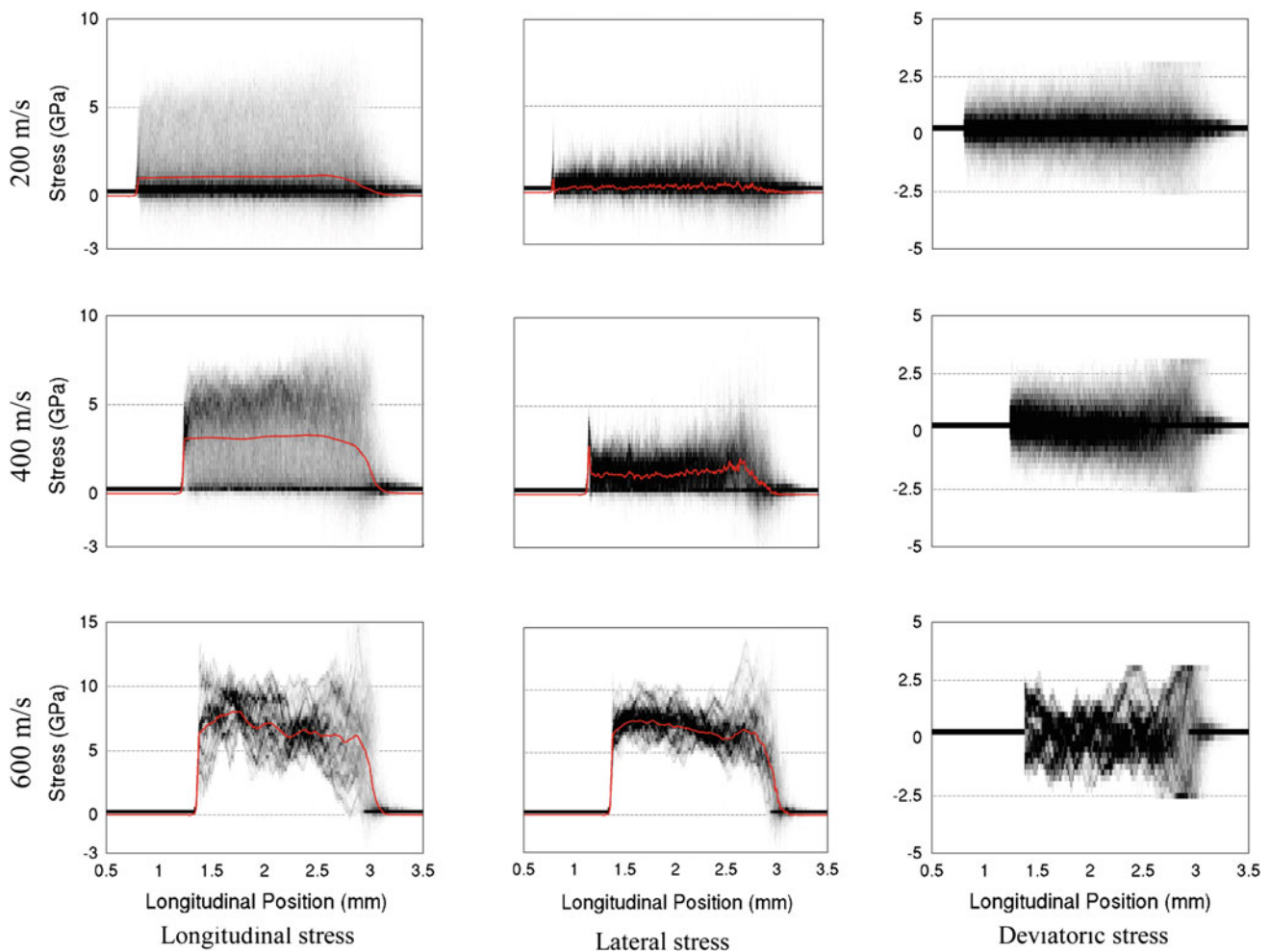


Fig. 13 Stress distribution from two-dimensional simulation with grain stiction. The *grey scale* indicates the range of stress states achieved whereas the *red line* indicates the average stress states achieved

wave, as the average stress develops to a steady wave. These variations occur near the leading edge of the compaction wave and can persist even after the steady state stress level has been achieved. This developing region is dominated by stress bridge formation and involves the grain rearrange as individual grains move before settling into a fixed position. In some instances, especially at high plate velocities, there are large deviations in stress during this rearrangement process, even significant occurrences of negative longitudinal stress. As an example, examine the compaction presented in Fig. 13 at 600 m/s. The initial rise in the steady state stress level profile of 7.5 GPa appears to be centered at about 3 mm, however there are significant occurrences of stress as high as 15 GPa in a region immediately behind the compaction wave front. This behavior can be observed in all the longitudinal stress profiles at a driver plate velocity of 600 m/s. Thus one should not assume that steady wave behavior is achieved once the average stress is achieved. There still appears to be some grain rearrangement underway. This behavior will

be discussed in greater detail in conjunction with the lateral velocity profiles.

3.7 Stress distributions

Figure 15 presents stress distributions that further illustrate the bi-modal nature of the stress states behind the compaction wave. Each computational cell that contains mass contributes one occurrence of stress. The occurrences of stress are then plotted as a histogram in order to obtain a distribution. The figures present distributions of the longitudinal, lateral and deviatoric stress states over a range of driver plate velocities. Data presented in these distributions were obtained from the data presented in Figs. 13 through 16 at a single longitudinal slice positioned 2.75 mm for the two-dimensional simulations and at 0.75 mm for the three-dimensional simulations.

The curves presented in Fig. 10 illustrate that the longitudinal stress smoothly increases as the drive plate velocity increases. However, the succession of longitudinal stress

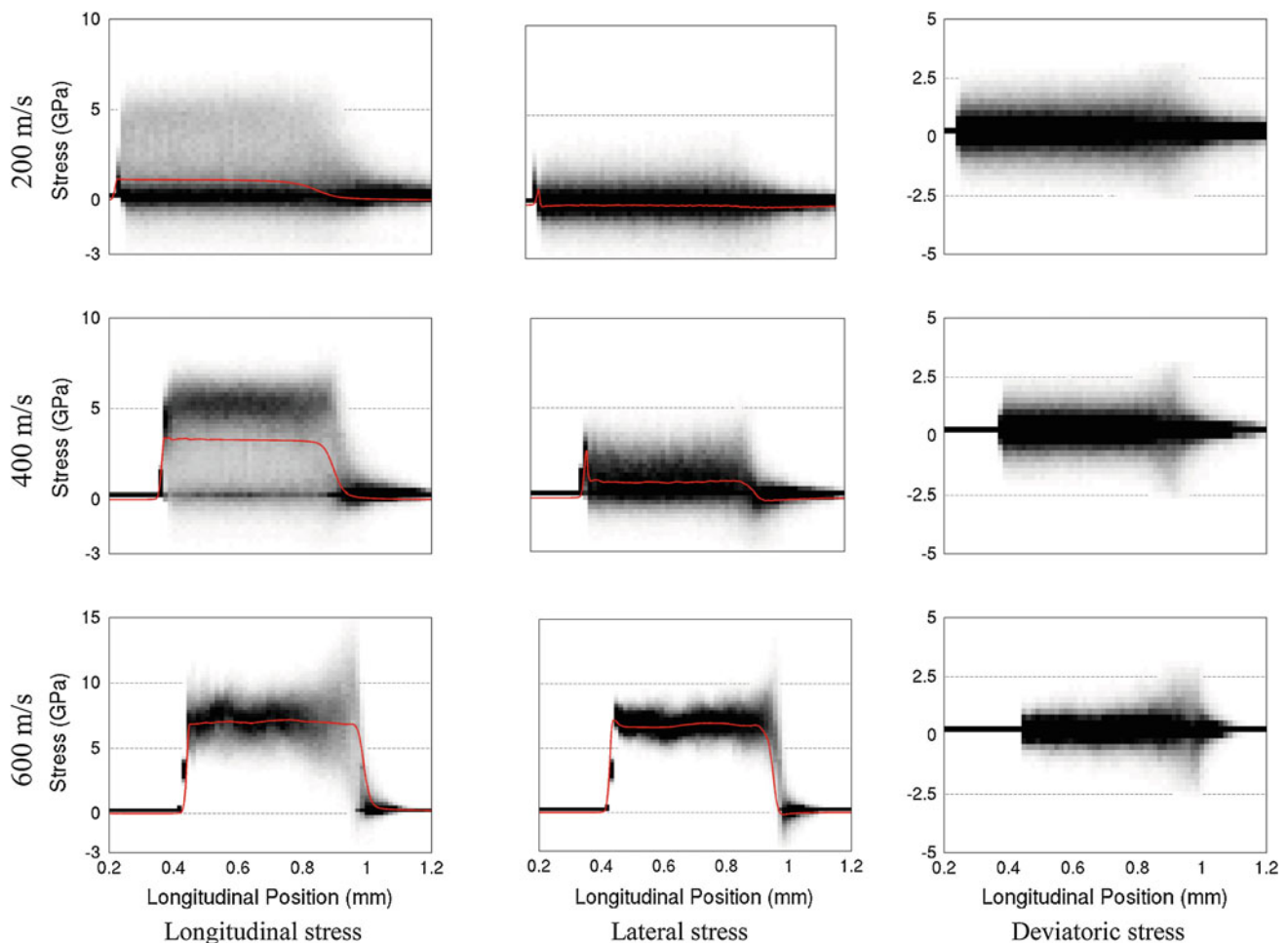


Fig. 14 Stress distribution from three-dimensional simulation with grain sliding. The *grey scale* indicates the range of stress states achieved whereas the *red line* indicates the average stress states achieved

distributions presented in Fig. 15 demonstrate that the evolution of the average stress is actually achieved through an exchange of modes, from a distribution centered near zero towards a distribution centered near the dynamic yield stress of 5 GPa. As the average stress exceeds the dynamic yield strength and all of the porosity is removed, a single distribution emerges and slides to the right, towards higher stress levels, as the driver plate velocity increases. For the three-dimensional simulations the emerged distribution appears normal (Gaussian), whereas for the two-dimensional simulations the emerged distribution does not appear normal.

The role of grains forming stress bridges (see Fig. 4) and grains outside the bridge network is better understood in the context of these distributions. Grains outside the force chain network experience little to no stress, thus they represent the stress distribution centered near zero. There are significant occurrences of negative (tensile) longitudinal stress. The grains that form stress bridges carry the load and are represented by the distributions centered about the dynamic

yield strength. The stress bridges form and persist until grains within the bridge yield and flow, locally alleviating stress. As the local grain network deforms new stress bridges are formed, and other grains are forced to bear significant stress. The presence and the dynamic nature of the stress bridges tends to maintain grains in a network at or near the local yield strength. Thus there are always significant portions of the grains involved in the stress network and are represented by the stress distribution near 5 GPa. The bulk average stress is simply the equilibrium struck between the loaded (stress bridge) and unloaded grains. This dynamic, where a stress network is established through local yield, takes place within the initial formation of the compaction wave, i.e., within the first 16 grains where there is significant deviatoric stress. Thereafter the stress network appears relatively stable.

As the driver plate velocity is increased the average bulk stress increases. The bimodal processes described above dominates the stress behavior. As Fig. 10 indicates the compaction behavior intersects the solid Hugoniot at roughly

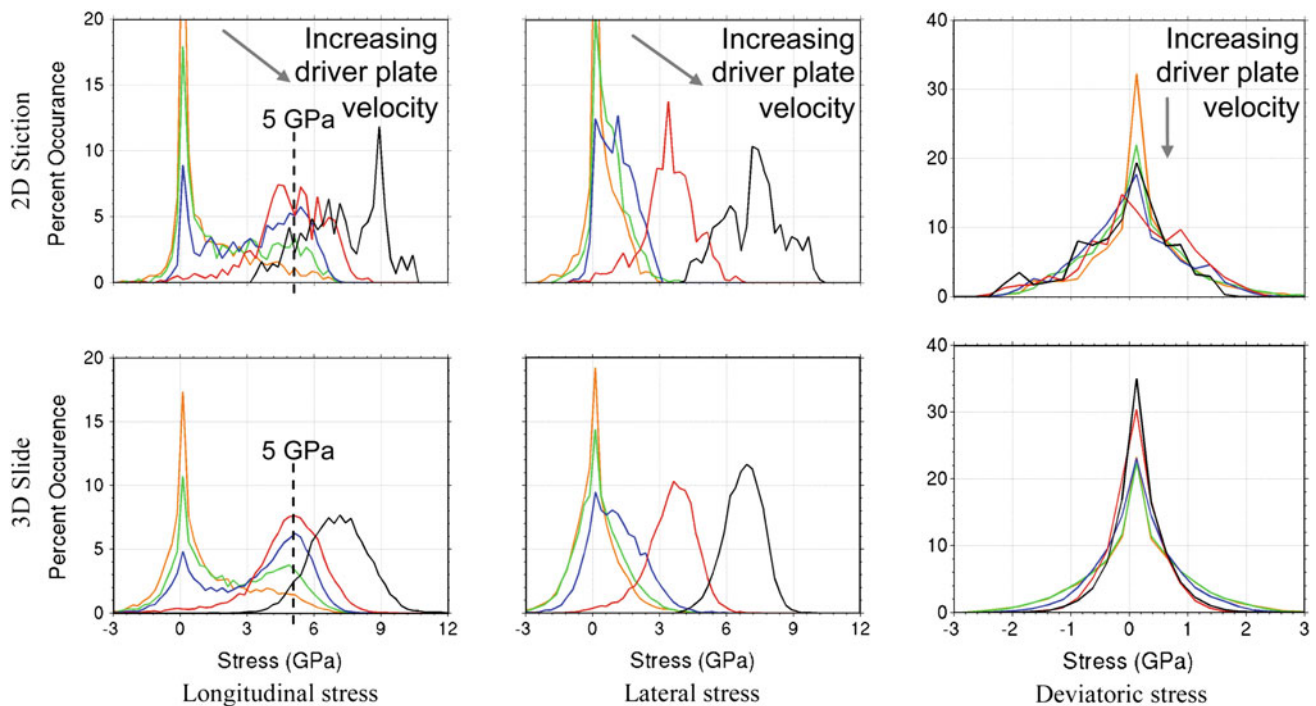


Fig. 15 Stress distributions as a function of driver plate velocity for velocities of 200 (orange), 300 (green), 400 (blue), 500 (red) and 600 m/s (black). Distributions were taken from the data presented in

the dynamic yield strength. This also represents the stress at which nearly all the porosity is removed and all of the grains experience a stress near the dynamic yield stress. Once all of the porosity is removed, Fig. 15 indicates that a near normal stress distribution emerges and translates to the right with increasing stress.

The evolution of the lateral stress is somewhat different than that of the longitudinal stress. The lateral stress appears bimodal but not to the same degree as the longitudinal stress. Rather, the average lateral stress appears to track the peak occurrence of the lateral stress distribution as it slides to the right. It is interesting to point out that the stress bridges appear as striations aligned in the longitudinal direction. Thus the formation of the stress bridge network is an essential feature associated with the exchange of modes centered near zero and the dynamic yield stress. This could account for the difference in the evolution behavior of the longitudinal and lateral stress distributions. Thus the lack of stress bridges in the lateral direction precludes a bimodal distribution. The average xy component of shear stress evolves much differently than either the lateral or longitudinal stress. The shape of the distributions do not appear Gaussian.

In general the stress distributions for the two-dimensional simulations are less smooth than the three-dimensional simulations in part because of the greater number of cells in the $0.75 \text{ mm} \times 0.75 \text{ mm}$ three-dimensional cross-section than in a 3 mm two-dimensional slice. In order to explore this

Figs. 13 and 14 at a single longitudinal position of 2.75 and 0.75 mm for the two- and three-dimensional simulations, respectively

further, we increased the lateral size of the domain to see if the two-dimensional simulations would yield distributions that would alter their shape and perhaps become smoother; Fig. 16 is the result for the 300 m/s simulations. The lateral domain was increased from 1 to 18 mm; the number of cells in the computation was also increased to maintain a constant resolution. The results indicate that although the stress distribution becomes somewhat more smooth, it maintains its basic shape. The only real difference occurs for the 1 mm domains where there is a drop cut-off in occurrence of high stress states.

3.8 Stress distribution comparison

Figure 17 presents stress distributions at three different driver plate velocities: 200, 400 and 600 m/s. These distributions were obtained by summing the occurrences of stress behind the entire compaction front, not simply obtained at a single longitudinal position behind the compaction front. As a result they are smoother than those presented in Fig. 15. Like the previous distributions, they only include computational cells involved in the compaction process; the driver plate and windows have been excluded. The longitudinally summed distributions obtained from the three-dimensional simulations are similar to the distributions obtained at a fixed longitudinal position, i.e., the basic shape of the distribution does not change as much along the longitudinal direction.

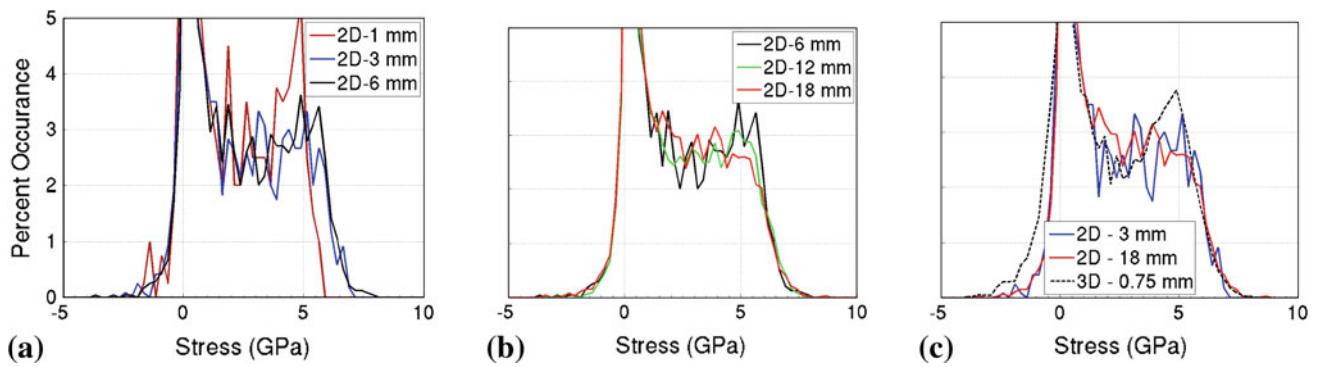


Fig. 16 Comparison of longitudinal stress distributions calculated from two- and three-dimensional simulations with varying domain width. Two-dimensional simulations were performed with stiction (Fig.

17, 2nd row first column) while three-dimensional simulations were performed with sliding, both at 300 m/s

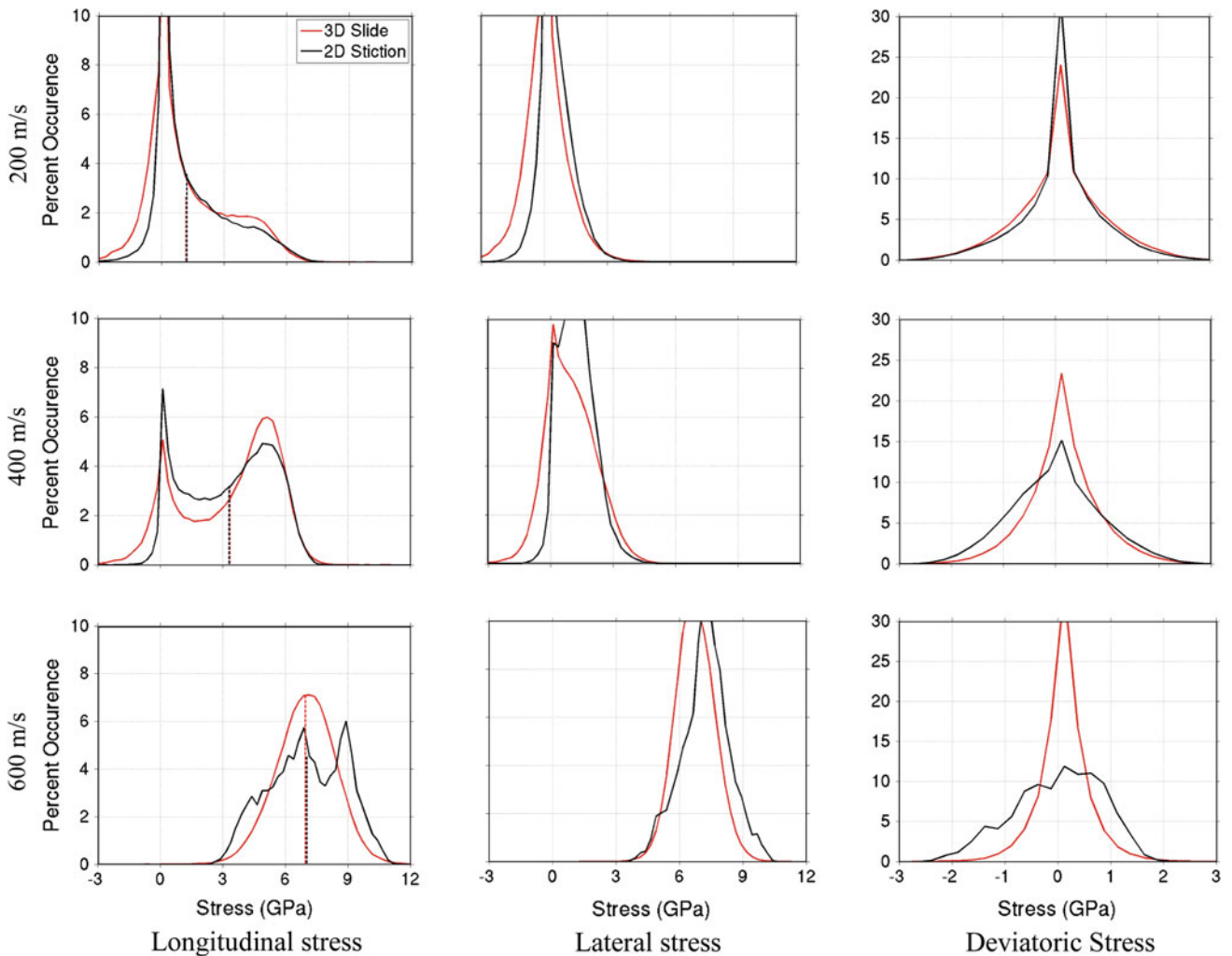


Fig. 17 Comparison of stress distributions. Distributions are obtained data obtained over a 0.3 mm window along the x -axis centered at 0.2 cm for the two-dimensional simulations and at 0.075 cm for the three-dimensional simulations

In Fig. 17, the average longitudinal stresses (i.e., the bulk Hugoniot stress) is included on the distributions as a vertical line. One can see that during the removal of porosity the average longitudinal stress does not corre-

spond to the most expected value of stress on the distribution; because of the bimodal nature of these stress distributions. The most obvious example of this is the 400 m/s driver plate velocity, where the porosity has not

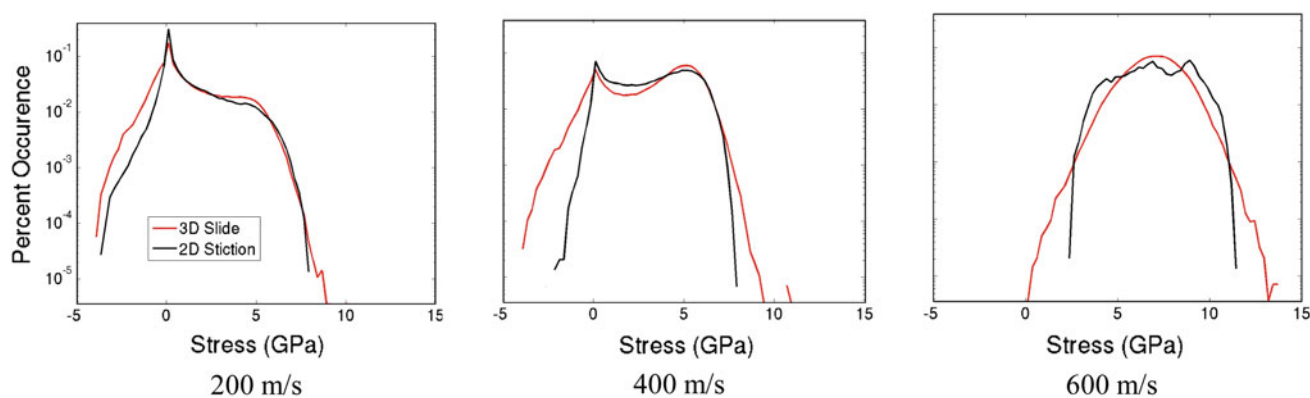


Fig. 18 Semi-log plot of longitudinal stress at three different driver plate velocities

been completely removed; the bulk averaged density is near 14.5 g/cm^3 . For this figure, the average longitudinal stress for the three-dimensional sliding simulation is 3.35 GPa, whereas the two-dimensional stiction stress is 3.31 GPa. Although the averages for these simulations is near 3.3 GPa the most expected value of stress exhibits two local maxima, one near zero and another greater than 5 GPa. At higher stress levels the average longitudinal stress approaches the most expected value on the distribution.

An interesting observation can be made when comparing these simulations. Figure 10 indicates that these two simulations produce comparable bulk stress over the entire range of driver plate velocities. However, as the driver plate velocity is increased the amplitude of the distributions differs even though the shape of the distribution remains similar. For example, the average stress-density for a driver plate of 400 m/s is 14.62 g/cm^3 and 3.31 GPa for the two-dimensional stiction simulations and 14.56 g/cm^3 and 3.35 GPa for the three-dimensional sliding simulations. Although these values are quite close, the amplitude of the expected values of their respective stress distributions differs. Figure 17 presents the difference in occurrence at higher stress states for the two-dimensional simulation as compared to the three-dimensional simulation. These figures indicate that at the extreme states within the distributions there are differences. Although not of much importance here, differences in the extreme states may be important in reacting or energetic materials.

In order to explore the differences of these stress distributions further, Fig. 18 presents the longitudinal stress distributions on a semi-log plot. Although, the bulk longitudinal stress for two-dimensional stiction and three-dimensional sliding simulations are similar, there exist differences in their stress distributions even at the highest stresses obtained in the simulation.

3.9 Velocity distributions

In order to better understand the structure of the compaction wave the lateral particle velocities from the simulations of interest are presented in Fig. 19 as a contour plot of occurrences. For each of these figures the lateral velocity has been non-dimensionalized by the driver plate velocity. These figures illustrate that there are regions of significant lateral particle motion, especially near the leading edge of the compaction front. The lateral velocity results in grain rearrangement near the leading edge of the compaction front followed by a region of reduced rearrangement. This region of initial high lateral velocity is correlated to the large deviatoric shear stress presented in Fig. 6. As the driver plate velocity is increased the lateral particle velocity, even after the leading edge rearrangement, remains significant. This is especially true as the driver plate velocity is increased. For the driver plate velocity of 600 m/s the porosity has been completely removed. Once porosity is completely removed, the grain rearrangement corresponds to what is essentially the onset of dissipation via turbulent mixing of the consolidated material. Since the entire grain ensemble has yielded the material can flow through lateral motion more readily.

A distinguishing feature of these simulations is the thickness of this rearrangement window near the leading edge of the compaction front. For flyer plate velocity of 400 m/s, the two-dimensional simulations result in a rearrangement window that is approximately 0.5 mm wide, whereas the corresponding rearrangement window for the three-dimensional simulations is less than 0.25 mm wide.

Figure 20 presents distributions of the dimensionless lateral velocity at driver plate velocities of 200, 400 and 600 m/s. These distributions were generated by summing the occurrences of lateral velocity in the rearrangement windows. The distributions indicate that the majority of the material experiences little to no lateral velocity as the compaction

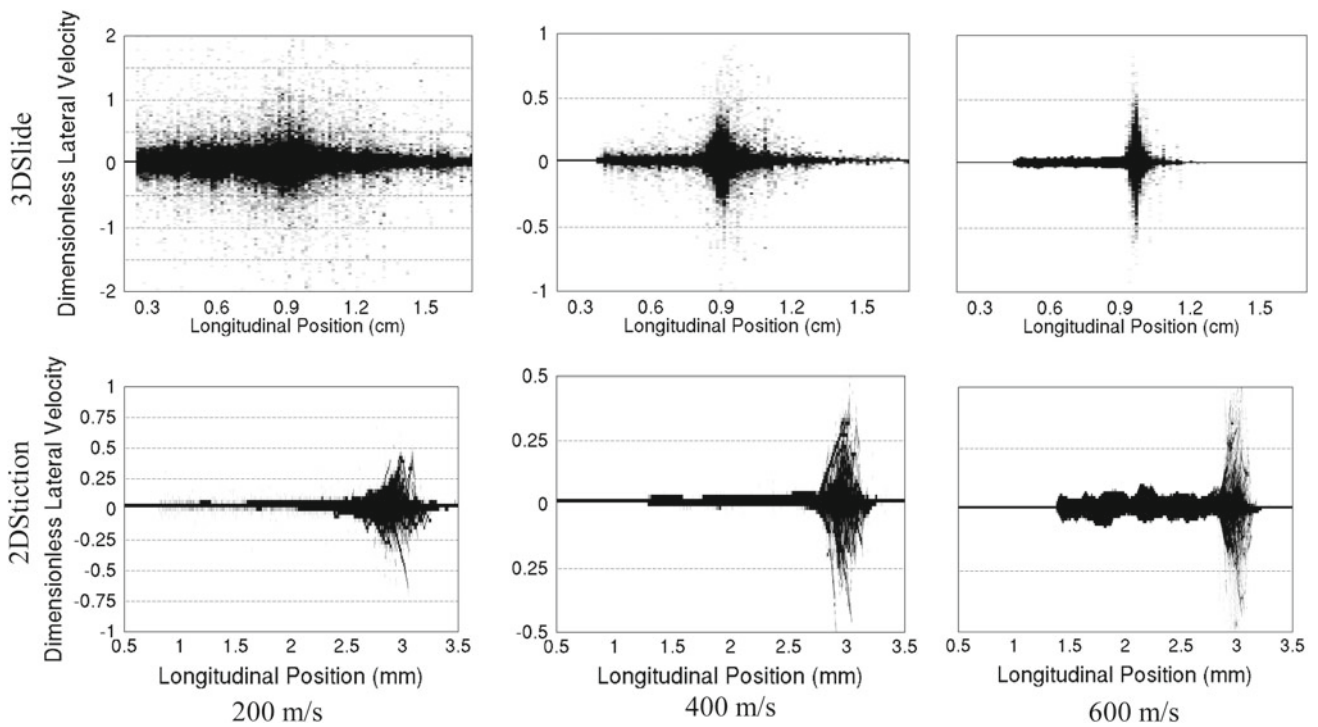


Fig. 19 Lateral velocity contours as a function of longitudinal position over a range of driver plate velocity

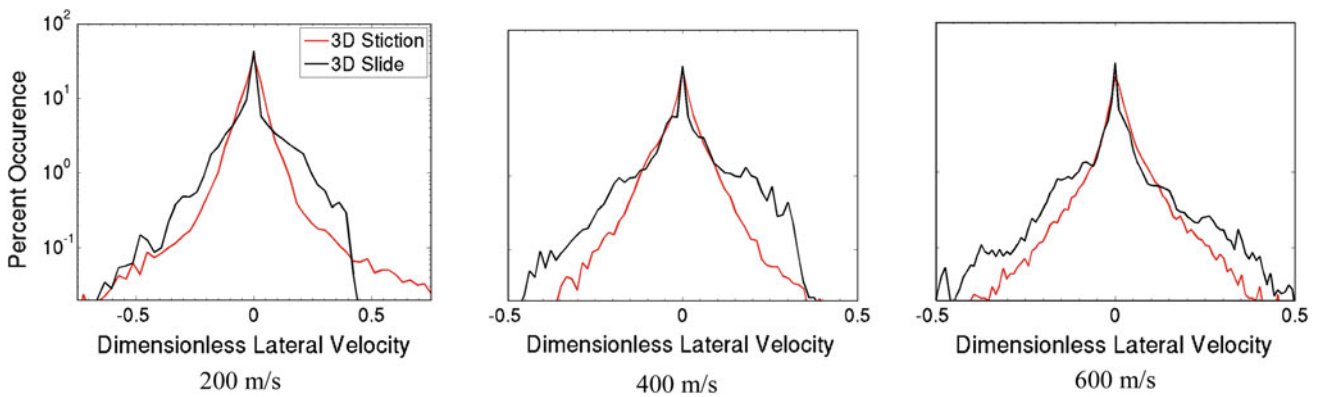


Fig. 20 Percent occurrence of lateral velocity for various driver plate velocities

wave passes. In general, the three-dimensional simulations experiences less lateral velocity than the two-dimensional simulations. One conclusion is that grains bound in a three-dimensional network, that are more likely to have multiple-points of contact with their nearest neighbors, would experience less lateral velocity than two-dimensional grains which might be free to move. Alternatively, it is possible that particles in the two-dimensional simulations either move left or right whereas particles in the three-dimensional simulations can move in any direction. Thus more freedom of direction could result lower lateral velocities. Further investigation would be needed in order to pinpoint the differences in lateral velocity for two- and three-dimensional simulations.

3.10 Temperature distributions

Thus far we have examined mechanical quantities such as stress or velocity. Although it is not typically as important for ceramics such as those studied here, temperatures are critically important for a variety of heterogeneous energetic materials [21, 22, 30]. Figure 21 presents contours of temperature occurrences as a function of longitudinal distance over a range of driver plate velocities. The variation in the temperature distributions is smoother than those for stress or lateral velocity. For example, there does not appear to be a large overshoot in the average temperature near the leading edge of the compaction front, as seen in stress or lateral velocity, yet a smooth rise from the initial temperature of 300 K. There

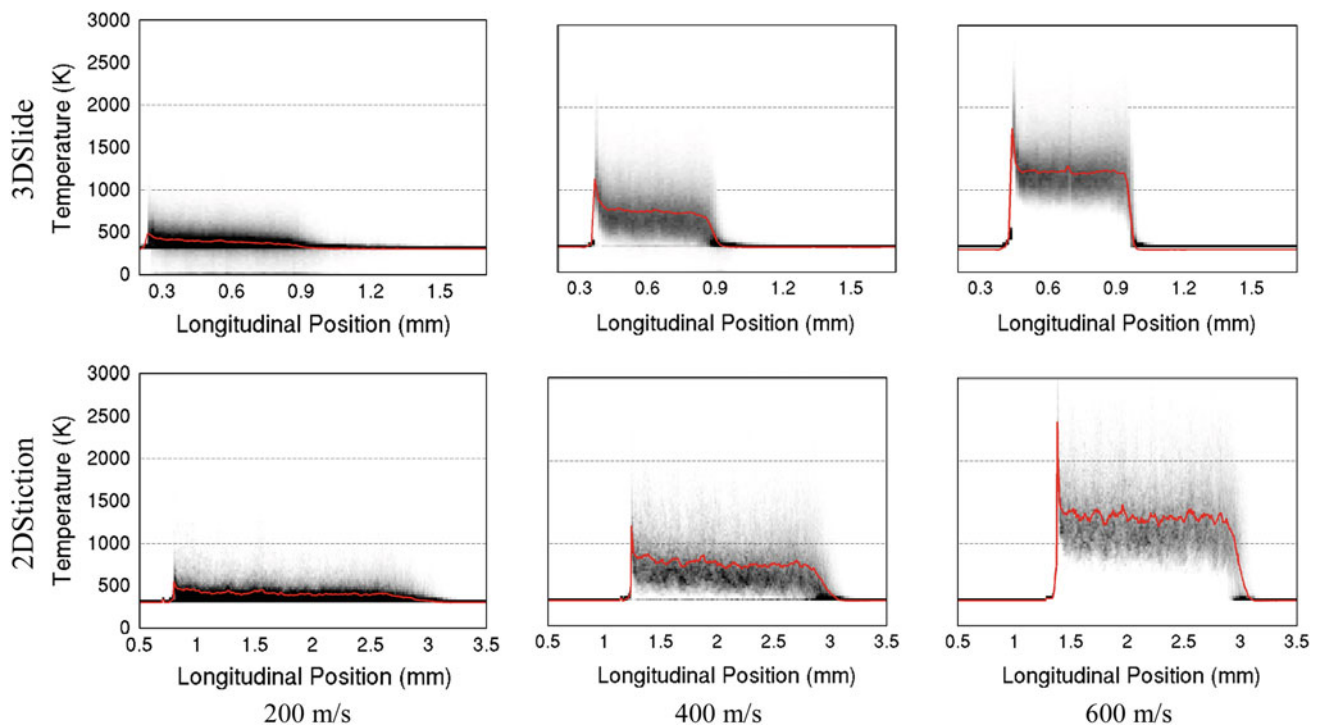


Fig. 21 Temperature contours as a function of longitudinal position over a range of driver plate velocity. The *grey scale* indicates the range of temperature states achieved whereas the *red line* indicates the average temperature states achieved

could exist a slight trend upward in average temperature as a function of lateral velocity; this can be seen in the 400 and 600 m/s simulations.

Figure 22 presents the temperature distributions obtained from driver plate velocities of 200, 400 and 600 m/s along with the tails of the distributions near the highest temperatures observed. When the granular material is compacted, a distribution of temperature emerges from 300 K and slides to the right as the driver plate velocity is increased. The temperature distributions are broadly spread about their average, with positive skew: the distributions have longer tails at higher temperatures. The temperature distributions demonstrate less of the bi-modal behavior exchange as a function of driver plate velocity as compared to the longitudinal stress distributions. This is due to the deformation mechanisms associated with increasing temperature. The heating of material due to volumetric compression is minimal at the pressures investigated here. The temperature is increased as grains yield and plastic stain work is accumulated. Grains not involved in the formation and deformation of stress bridges do not significantly increase in temperature. The effect of friction is not included in these simulations however it could be important locally. The distribution indicates that not until all the porosity is removed and every grain experiences deformation are there no occurrences of temperature at 300 K.

Like stress, the three-dimensional distributions of temperature are smoother than their two-dimensional counter-

parts. The average temperature, for each distribution, has been indicated with a vertical line. For example the average temperatures for a driver plate velocity of 400 m/s are 703 and 760 K for the three-dimensional sliding and two-dimensional stiction cases, respectively. Unlike longitudinal stress, the average temperature is closer to the most expected value of temperature. In nearly all simulations, the two-dimensional simulations have higher average temperatures than their three-dimensional counterparts. Across a range of driver plate velocities, the two-dimensional stiction simulations show a 6 % higher average temperature than the three-dimensional sliding simulations. This trend of higher temperatures in two-dimensions persists at the highest temperatures as well; there are more occurrences of very high temperatures for the two-dimensional simulations as compared to the three-dimensional simulations. With regard to energetic and reacting systems, where the sensitivity of a reacting mixture might depend heavily upon the peak temperature obtained with a representative volume, two-dimensional simulations might represent an upper bound.

4 Discussion

To our knowledge this is the first systematic comparative mesoscale study of the dynamic compaction of two-dimensional versus three-dimensional heterogeneous granular systems with stiction versus sliding. More work

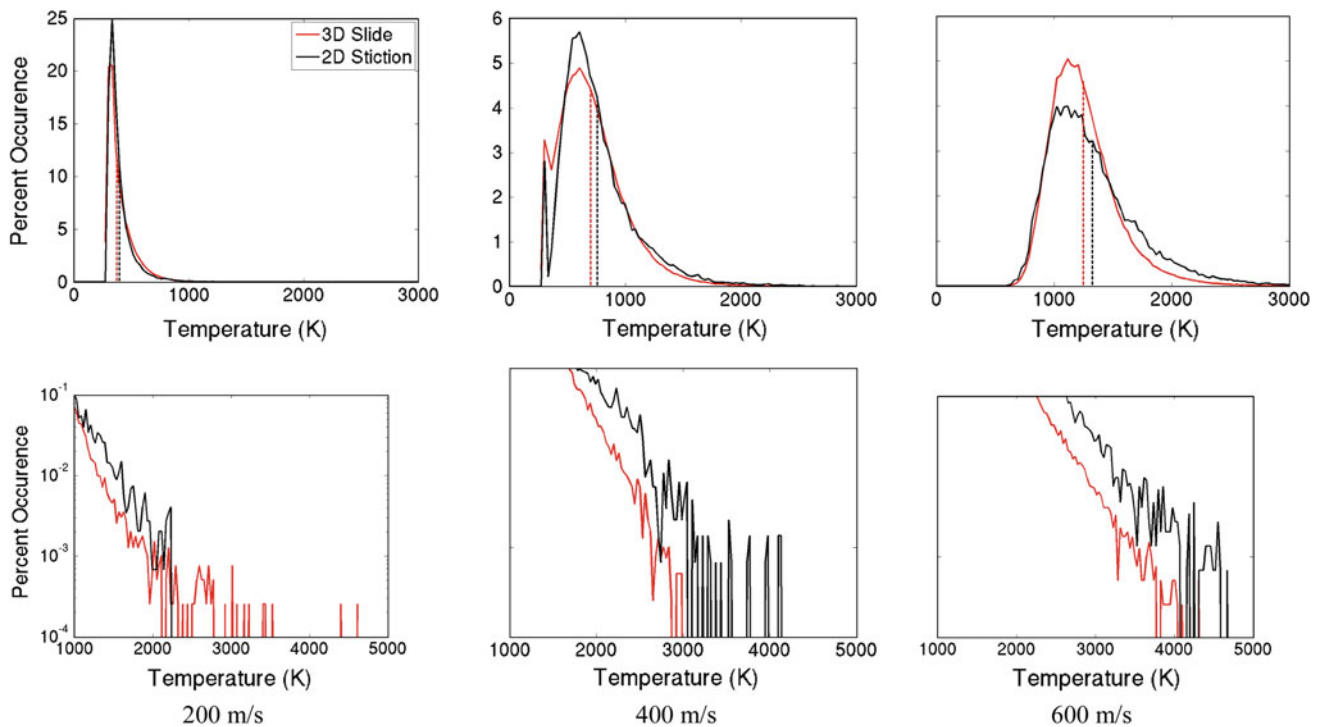


Fig. 22 Percent occurrence of temperature for various driver plate velocities

in this area is needed in order to make general statements regarding the applicability of these results across a wide range of materials, forms of heterogeneity and initial pack densities. The result presented here are not consistent with dynamic compaction results for other classes of heterogeneity. For example, at higher pack densities such as those encountered with filled heterogeneous energetic systems, the structure of the compaction wave is quite different than what was observed here. For example, the sliding versus stiction boundary condition does not affect the Hugoniot response of epoxy filled WC [62]. At lower pack densities, two-dimensional simulations can under-predicting the shock velocity because extreme distension results in snow-plow behavior [63]. Thus further investigations are necessary in order to draw informed generalizations.

Although there are differences in the two- and three-dimensional simulations, the usefulness of both is evident. A significant finding of this work is that in order to simulate the bulk longitudinal stress behavior of dry WC at roughly the pour density accurately, one must initially weld the grain realizations in two-dimensional simulations and allow sliding (minimize the friction) in three-dimensional simulations. If one is seeking the bulk longitudinal stress (bulk stress), then a two-dimensional planar simulation over a range of particle velocities is a comparatively easy computation to perform and may provide adequate results. For the simulations presented here a typical two-dimensional simulation (3.5 million cells) requires 841 core hours of CPU time whereas a three-dimensional simulation (55 million cells)

requires 11,185 core hours time, a 10-fold increase in computational resources. This does not account for the fact that the two-dimensional simulations are twice as long in the longitudinal direction and therefore ran for nearly twice as long which could be important for processes that occur over a finite time scale such as a shock to detonation transition. The result is there is considerable computational saving in running two-dimensional simulations as compared to three-dimensional simulations. Thus two-dimensional simulations are achievable with high-end desktop computers, whereas the three-dimensional simulations are only achievable with moderate-sized cluster computers.

It is worth noting that although two- and three-dimensional simulations produce nearly the same prediction of bulk stress, differences do appear in their stress and temperature distributions, especially at the extremes. For example, there is a greater occurrence of high temperature cells for two-dimensional simulations as compared to the three-dimensional simulation. These differences do not necessarily diminish as the two-dimensional simulations increase in domain size but appear to be fundamental to the natures of two- and three-dimensional simulations. Differences between the two and three-dimensional simulations are further highlighted in the stress–strain rate relationship. Like bulk stress, these trends can be compared to experimental data for validation. The three-dimensional sliding simulations most closely reproduced the experimentally measured stress–strain rate relationship for rise times.

Although this work illustrates some differences between two- and three-dimensional simulations, these differences are not universally true of all heterogeneous systems. For example mesoscale simulations of fully consolidated heterogeneous materials, such as reactive materials, have demonstrated the two-dimensional simulations reproduce the same bulk response for both two- and three-dimensional simulations, irrespective of grain contact conditions. The nature and evolution of these systems are fundamentally different from the systems investigated here. For example, difference in out-of-plane strength is captured within a two-dimensional simulation of a fully consolidated heterogeneous system. In addition there are differences that can be attributed to the role of pore collapse and jetting, impedance and strength mismatch, as well as the ability of a soft binder to take up and average the load around harder grain network. Thus the simulations presented here, and the observations therein, should remain in the context of porous granular systems; extrapolation of these results to other heterogeneous systems or identical systems at higher pressure may not be appropriate.

Another significant finding of this work is the mechanism by which the bulk stress increases as the driver plate velocity increases. The bulk stress increases through an exchange of modes or distributions: one distribution centered about zero and one distribution centered about the dynamic flow stress. This exchange is facilitated through the formation of longitudinally oriented stress bridges. Other state variables such as lateral stress, temperature and lateral velocity do not exhibit an exchange of modes to the same degree. However, this exchange of modes means that the average stress is not necessarily well representing the stress within the stress bridge network. This points to a new way of looking at the dynamic nature of porous granular systems, and perhaps new modeling formulations.

5 Conclusions

In this investigation we have performed the first detailed comparisons of the results obtained from two- and three-dimensional mesoscale simulations of granular materials. We know of no other careful comparison between two- and three-dimensional calculations. While one must be cautious in extrapolating results from a study focused on a particular material and utilizing a certain numerical technique to other material or techniques, we believe that these results should prove useful in those cases as well. The role of grain contact and friction is an essential mechanism in the dynamic compaction of loose dry granular materials. The sliding and stiction conditions investigated here represent the extreme behaviors of friction. In this work, it was found that one can accurately simulate the bulk longitudinal stress by initially welding the grain realizations in two-dimensional

simulations or minimizing the friction in three-dimensional simulations. The welding of grains in a two-dimensional simulation seems to replicate the strength provided by the out-of-plane network of interlocking grains. The bimodal nature of the longitudinal stress distributions, the exchange of modes and the emergence of near normal distributions is an interesting feature of these simulations. Two- and three-dimensional simulations do yield somewhat different results when the distributions of thermodynamic and mechanical states are compared. This is especially true at the extreme end of these states. However, the two-dimensional simulations not only accurately simulate the experimental bulk compaction response but faithfully reproduce the trends in the stress–strain rate behavior. The two-dimensional simulations yield distributions of lateral and deviatoric stress, lateral velocity and temperature that are similar to those obtained from the three-dimensional simulations. It remains to be seen if these differences are experimentally quantifiable and/or significant in the dynamic evolution of loose dry granular systems. The significantly greater computational costs associated with the three-dimensional calculations must be balanced against the modest differences between the two- and three-dimensional cases, particularly in light of shortcomings that might be present in the three-dimensional simulations.

Acknowledgments Sandia National Laboratories is a multi-program laboratory managed and operated by Sandia Corporation, a wholly owned subsidiary of Lockheed Martin Corporation, for the U.S. Department of Energy's National Nuclear Security Administration under contract DE-AC04-94AL85000.

References

1. Carroll, M.M., Holt, A.C.: Static and dynamic pore-collapse relations for ductile porous materials. *J. Appl. Phys.* **43**, 1626–1636 (1972)
2. Asay, J.R., Shahinpoor, M.: *High-Pressure Shock Compression of Solids*, p. 7. Springer, Berlin (1993)
3. Hermann, W.: Constitutive equation for the dynamic compaction of ductile porous materials. *J. Appl. Phys.* **40**(6), 2490–2499 (1969)
4. Grady, D.E., Winfree, N.A.: A computational model for polyurethane foam. In: Staudhammer, K.P., Murr, L.E., Meyers, M.A. (eds.) *Fundamental Issues and Applications of Shock-Wave and High-Strain-Rate Phenomena*. Proceedings of EXPLOMET, pp. 485–491 (2001)
5. Benson, D.J., Nellis, W.J.: Dynamic compaction of copper powder: computation and experiment. *Appl. Phys. Lett.* **65**, 418–420 (1994)
6. Benson, D.J.: An analysis by direct numerical simulation of the effects of particle morphology on the shock compaction of copper powder. *Model. Simulation Mater. Sci. Eng.* **2**, 535–550 (1994)
7. Benson, D.J.: The calculation of the shock velocity: particle velocity relationship for a copper powder by direct numerical simulation. *Wave Motion* **21**, 85–99 (1995)
8. Benson, D.J., Nesterenko, V.F., Jonsdottir, F.F., Meyers, M.A.: Quasistatic and dynamic regimes of granular material deformation under impulse loading. *J. Mech. Phys. Solids* **45**(11), 1955–1999 (1997)

9. Williamson, R.J.: Parametric studies of dynamic powder consolidation using a particle-level numerical model. *J. Appl. Phys.* **68**, 1287–1294 (1990)
10. Horie, Y., Yano, K.: Non-equilibrium fluctuations in shock compression of polycrystalline α -iron. In: Furnish, M.D., Thadhani, N.N., Horie, Y. (eds.) *Shock Compaction of Condensed Matter-2001*, pp. 553–556 (2002)
11. Case, S., Horie, Y.: Mesoscale modeling of the response of alumina. In: Furnish, M.D., Elert, M., Russell, T.P., White, C.T. (eds.) *Shock Compression of Condensed Matter-2005*, pp. 299–302 (2005)
12. Bourne, N.K.: Modelling the shock response of polycrystals at the mesoscale. In: Furnish, M.D., Elert, M., Russell, T.P., White, C.T. (eds.) *Shock Compression of Condensed Matter-2005*, pp. 307–310 (2005)
13. Herbold, E.B., Cai, J., Benson, D.J., Nesterenko, V.F.: Simulation of Particle Size Effect on Dynamic Properties and Fracture of PTFE-W-Al Composites. In: Elert, M., Furnish, M.D., Chau, R., Holmes, N., Nguyen, J. (eds.) *Shock Compression of Condensed Matter-2007*, pp. 785–788 (2007)
14. Yano, K., Horie, Y.: Discrete-element modeling of shock compression of polycrystalline copper. *Phys. Rev. B* **59**, 13672–13680 (1999)
15. Nesterenko, V.F.: *Dynamics of Heterogeneous Materials*. Springer, Berlin (2001)
16. Meyers, M.A., Benson, D.J., Olevsky, E.A.: Shock consolidation: microstructurally-based analysis and computational modeling. *Acta Mater.* **47**, 2089–2108 (1999)
17. Crawford, D.A.: Using mesoscale modeling to investigate the role of material heterogeneity in geologic and planetary materials. In: Furnish, M.D., Elert, M., Russell, T.P., White, C.T. (eds.) *Shock Compression of Condensed Matter-2005*, pp. 1453–1457. AIP Press (2005)
18. Conley, P.A., Benson, D.J.: An estimate of the linear strain rate dependence of octahydro-1,3,5,7-tetranitro-1,3,5,7-tetrazocine. *J. Appl. Phys.* **86**, 6717–6728 (1999)
19. Ripley, R., Zhang, F., Lien, F.-S.: Acceleration and heating of metal particles in condensed explosive detonation. In: Elert, M., Furnish, M.D., Chau, R., Holmes, N., Nguyen, J. (eds.) *Shock Compression of Condensed Matter-2007*, pp. 409–412 (2007)
20. Do, I.P.H., Benson, D.J.: Micromechanical modeling of shock-induced chemical reactions in heterogeneous multi-material powder mixtures. *Int. J. Plasticity* **17**, 641–668 (2001)
21. Baer, M.R.: Modeling heterogeneous energetic materials at the mesoscale. *Thermochim. Acta* **384**, 351–367 (2002)
22. Baer, M.R., Trott, W.M.: Mesoscale descriptions of shock loaded heterogeneous porous materials. In: Furnish, M.D., Thadhani, N.N., Horie, Y. (eds.) *Shock Compression of Condensed Matter-2001*, pp. 713–716 (2002)
23. Menikoff, R.: Compaction wave profiles: simulations of gas gun experiments. *J. Appl. Phys.* **90**, 1754–1760 (2001)
24. Eakins, D.E., Thadhani, N.N.: Shock compression of reactive powder mixtures. *Int. Mater. Rev.* **54**(4), 181–213 (2009)
25. Milne, A.M., Bourne, N.K., Millett, J.C.F.: On the un-reacted Hugoniot of three plastic bonded explosives. In: Furnish, M.D., Elert, M., Russell, T.P., White, C.T. (eds.) *Shock Compression of Condensed Matter-2005*, pp. 175–178 (2006)
26. Benson, D.J., Conley, P.: Eulerian finite-element simulations of experimentally acquired HMX microstructures. *Model. Simul. Mater. Sci. Eng.* **7**, 333–354 (1999)
27. Lowe, C.A., Greenaway, M.W.: Compaction processes in granular beds composed of different particle sizes. *J. Appl. Phys.* **98**, 123519 (2005)
28. Benson, D.J., Do, I., Meyers, M.A.: Computational modeling of shock compression of powders. In: Furnish, M.D., Thadhani, N.N., Horie, Y. (eds.) *Shock Compression of Condensed Matter-2001*, pp. 1087–1092 (2001)
29. Tang, Z.P., Wang, W.W.: Discrete element modeling for shock processes of heterogeneous materials. In: Furnish, M.D., Thadhani, N.N., Horie, Y. (eds.) *Shock Compression of Condensed Matter-2001*, pp. 679–684 (2001)
30. Baer, M.R.: Mesoscale modeling of shocks in heterogeneous reactive materials. In: Horie, Y. (eds.) *Shock Wave Science and Technology Reference Library*, V2, pp. 321–356 (2007)
31. Trott, W.M., Baer, M.R., Castañeda, J.N., Chhabildas, L.C., Asay, J.R.: Investigation of the mesoscopic scale response of low-density pressings of granular sugar under impact. *J. Appl. Phys.* **101**(024917), 1–21 (2007)
32. Barua, A., Zhou, M.: A Lagrangian framework for analyzing microstructural level response of polymer-bonded explosives. *Model. Simul. Mater. Sci. Eng.* **19**(055001), 1–24 (2011)
33. Benson, D.J., Tong, W., Ravichandran, G.: Particle-level modeling of dynamic consolidation of Ti-SiC powders. *Model. Simul. Mater. Sci. Eng.* **3**, 771–796 (1995)
34. Meyers, M.A., Benson, D.J., Olevsky, E.: A shock consolidation: microstructurally-based analysis and computational modeling. *Acta Mater.* **47**(7), 2089–2108 (1999)
35. Borg, J.P., Vogler, T.J.: Mesoscale calculations of the dynamic behavior of a granular ceramic. *Int. J. Solids Struct.* **45**, 1676–1696 (2008)
36. Borg, J.P., Vogler, T.J.: Aspects of simulating the dynamic compaction of a granular ceramic. *Model. Simul. Mater. Sci. Eng.* **17**, 045003 (2009)
37. Vogler, T.J., Borg, J.P.: Mesoscale and continuum calculations of wave profiles for shock-loaded granular ceramics. In: Elert, M., Furnish, M.D., Chau, R., Holmes, N., Nguyen, J. (eds.) *Shock Compression of Condensed Matter-2007*, pp. 773–776 (2007)
38. Vogler, T., Borg, J.P., Grady, D.: On the scaling of steady structured waves in heterogeneous materials. *J. Appl. Phys.* (submitted)
39. Tong, W., Ravichandran, F., Christman, T., Vreeland, T.: Processing SiC-particulate reinforced titanium-based metal matrix composites by shock wave consolidation. *Acta Mater.* **43**, 230–250 (1995)
40. Reaugh, J.E.: *Grain-Scale Dynamics in Explosives*. Lawrence Livermore National Laboratory, UCRL-ID-150388, pp. 1–56 (2002)
41. Vorobiev, O.: Discrete and continuum methods for numerical simulations of non-linear wave propagation in discontinuous media. *Int. J. Numeric Methods Eng.* **83**, 482–507 (2010)
42. Dwivedi, S.K., Teeter, R.D., Felice, C.W., Gupta, Y.M.: Two dimensional mesoscale simulations of projectile instability during penetration in dry sand. *J. Appl. Phys.* **104**(083502), 1–15 (2008)
43. Vogler, T.J., Lee, M.Y., Grady, D.E.: Static and dynamic compaction of ceramic powders. *Int. J. Solids Struct.* **44**, 636–658 (2007)
44. McGlaum, J.M., Thompson, S.L., Elrick, M.G.: CTH: a three-dimensional shock wave physics code. *Int. J. Impact Eng.* **10**, 351–360 (1990)
45. Meyers, M.A.: *Dynamic Behavior of Materials*. Wiley-Interscience, New York (1994)
46. Austin, R.A., McDowell, D.L., Benson, D.J.: Numerical simulation of shock wave propagation in spatially-resolved particle systems. *Model. Simul. Mater. Sci. Eng.* **14**, 537–561 (2006)
47. Rice, M.H., McQueen, R.G., Walsh, J.M.: Compression of solids by strong shock waves. *Solid State Phys.* **6**, 1–63 (1958)
48. Dandekar, D.P., Grady, D.E.: Shock equation of state and dynamic strength of tungsten carbide. In: *Shock Compression of Condensed Matter-2001*, pp. 783–786 (2001)
49. Dandekar, D.P.: Spall strength of tungsten carbide. *Army Research Laboratory ARL-TR-3335*, pp. 1–22 (2004)
50. Steinberg, D.J.: Equation of state and strength properties of selected materials. *Lawrence Livermore National Laboratory, UCRL-MA-106439*, pp. 1–122 (1991)

51. Johnson, G.R., Cook, W.H.: Fracture characteristics of three metals subjected to various strains, strain rates, temperatures and pressures. *Eng. Fract. Mech.* **21**, 31–48 (1985)
52. Davison, L., Graham, R.A.: Shock compression of solids. *Phys. Rep.* **55**, 255–379 (1979)
53. Moshe, E., Eliezer, S., Dekel, E., Ludmirsky, A., Henis, Z., Werdiger, M., Goldberg, I.B.: An increase of the spall strength in aluminum, copper, and Metglas at strain rates larger than 10^7 s^{-1} . *J. Appl. Phys.* **83**, 4004–4011 (1998)
54. Graham, R.A.: *Solids under High-Pressure Shock Compression*. Springer, Berlin (1992)
55. Bardenhagen, S.G., Brackbill, J.U.: Dynamic stress bridging in granular material. *J. Appl. Phys.* **83**, 5732–5740 (1998)
56. Roessig, K.M., Foster, J.C.: Experimental simulations of dynamic stress bridging in plastic bonded explosives. In: Furnish, M.D., Thadhani, N.N., Horie, Y. (eds.) *Shock Compression of Condensed Matter-2001*, pp. 829–832 (2001)
57. Neal, W.D., Chapman, D.J., Proud, W.G.: The effect of particle size on the shock compaction of a quasi-mono-disperse brittle granular material. In: Elert, M.L., Buttler, W.T., Borg, J.P., Jordan, J.L., Vogler, T.J. (eds.) *Shock Compression of Condensed Matter-2011*. Proc AIP Conference, pp. 1443–1447 (2012)
58. Swegle, J.W., Grady, D.E.: Shock viscosity and the prediction of shock wave rise times. *J. Appl. Phys.* **58**, 692–701 (1985)
59. Zhuang, S., Ravichandran, G., Grady, D.E.: An experimental investigation of shock wave propagating in periodically layered composites. *J. Mech. Phys. Solids* **51**, 245–265 (2003)
60. Brown, J.L., Vogler, T.J., Grady, D.E., Reinhart, W.D., Chhabildas, L.C., Thornhill, T.F.: Dynamic compaction of sand. In: *Shock Compression of Condensed Matter-2001*, pp. 1363–1366 (2007)
61. Grady, D.E.: Structured shock waves and the fourth-power law. *J. Appl. Phys.* **107**(013506), 1–13 (2010)
62. Vogler, T.J., Alexander, C.S., Wise, J.L., Montgomery, S.T.: Dynamic behavior of tungsten carbide and alumina filled epoxy composites. *J. Appl. Phys.* **107**(4), 043520 1–13 (2010)
63. Borg, J.P., Chapman, D.J., Tsembelis, K., Proud, W.G., Cogar, J.R.: Dynamic compaction of porous silica powder. *J. Appl. Phys.* **98**(7), 073509, 1–9 (2005)